Buckling-induced interaction between circular inclusions in an infinite thin plate

Oz Oshri [1,*] Santidan Biswas,[2] and Anna C. Balazs[2]

[1]*Department of Mechanical Engineering, Ben-Gurion University of the Negev, Beer-Sheva 84105, Israel*

[2]*Chemical Engineering Department, University of Pittsburgh, Pittsburgh, Pennsylvania 15261, USA*

(Received 20 March 2020; accepted 14 August 2020; published 16 September 2020)

Design of slender artificial materials and morphogenesis of thin biological tissues typically involve stimulation of isolated regions (inclusions) in the growing body. These inclusions apply internal stresses on their surrounding areas that are ultimately relaxed by out-of-plane deformation (buckling). We utilize the Föppl-von Kármán model to analyze the interaction between two circular inclusions in an infinite plate that their centers are separated a distance of 2ℓ. In particular, we investigate a region in phase space where buckling occurs at a narrow transition layer of length ℓ_D around the radius of the inclusion, R ($\ell_D \ll R$). We show that the latter length scale defines two regions within the system, the close separation region, $\ell - R \sim \ell_D$, where the transition layers of the two inclusions approximately coalesce, and the far separation region, $\ell - R \gg \ell_D$. While the interaction energy decays exponentially in the latter region, $E_{\text{int}} \propto e^{-(\ell-R)/\ell_D}$, it presents nonmonotonic behavior in the former region. While this exponential decay is predicted by our analytical analysis and agrees with the numerical observations, the close separation region is treated only numerically. In particular, we utilize the numerical investigation to explore two different scenarios within the final configuration: The first where the two inclusions buckle in the same direction (up-up solution) and the second where the two inclusions buckle in opposite directions (up-down solution). We show that the up-down solution is always energetically favorable over the up-up solution. In addition, we point to a curious symmetry breaking within the up-down scenario; we show that this solution becomes asymmetric in the close separation region.

DOI: 10.1103/PhysRevE.102.033004

I. INTRODUCTION

Inclusions in solid bodies are isolated regions of inhomogeneities that encompass different elastic constants or eigenstrains, i.e., strains produced without external forces. Although the study of these inclusions has a long history in structural mechanics, dating back to the foundational work by Eshelby [1,2], the topic has recently regained interest in the context of the modeling of softer, biological, and synthetic materials. In biology, the morphogenesis of soft materials typically involves the addition of mass into isolated regions of the growing body. These isolated regions alter the elastic response of the material and its rest configuration and therefore effectively behave as Eshelby's inclusions. In fact, the latter reorientation of the current (reference) configuration was identified as a key factor in the mechanics of growing bodies [3,4]. When this reorientation does not preserve the body's integrity (i.e., necessary continuity constraints), internal strains are accommodated around the area of the inclusion and drive the system out of equilibrium. Relaxation of these strains are then associated with growth, i.e., the process in which the body obtains its shape.

While inclusions in three-dimensional (3D) solids require relatively large eigenstrains to deform the entire body, thin sheets, which are almost 2D structures, undergo pronounced 2D-to-3D shape transitions on relatively small stimulation. This inclusion-based deformation of thin materials has recently been of interest in various technological applications. For example, electrical actuators embedded in specific regions of thin origami structures behaved as isolated inclusions, i.e., they produced localized internal stresses that drove the system into different, desired shapes [5]. Artificial materials, such as thin layers of gels, are often designed using discontinuous variations of the cross-linked density [6–11]. On actuation, these islands of discontinuities swell to a different degree than their surrounding areas, thereby allowing the creation of complex configurations. Another example is given in Refs. [12,13], where two dimensional network of Hookean springs is used to design metamaterials with memory effects. Within these discrete models, isolated springs in the network (inclusions) are endowed with different rest lengths. These network's impurities then promote buckling of isolated regions that reshape the entire membrane. In nature, embedded fibers behave as slender elongated inclusions in organic materials. Their relatively high stiffness, compared with the surrounding matrix, allows plants to change their shapes due to the application of external stimuli [14,15].

Many of the aforementioned applications utilized several inclusions to control the global deformation of the body. Therefore, appropriate modeling of these systems must take into consideration how neighboring inclusions can interact cooperatively and undergo mutual deformation [10]. Although elastic bodies that contain multiple inclusions have been studied extensively, either in the framework of linear elasticity [2,16] (with an emphasis on 2D plane-strain configurations

*oshrioz@bgu.ac.il

[17]) or in the context of fluid membranes [18–21], less attention has been given to the effects of these interactions in thin elastic plates [22,23]. These plates couple stretching and bending deformations and are analytically described in the framework of the Föppl-von Kármán (FvK) model and the extension of this theory [4,24–27]. In general, this coupling between in-plane and out-of-plane deformations adds nonlinear terms to the theory that allow the coexistence of multiple solutions under the same setup of external confinements.

Some general guidelines to the postbuckling behavior of thin plates were presented by Davidovitch *et al.* in a series of publications [28–31]. In a recent paper [32], we utilized these insights to investigate the behavior of a circular inclusion with positive eigenstrain in a plate with thickness h. Our main findings were summarized on a bendability-confinement state diagram. While bendability measures the plate's slenderness, R/h, where R is the inclusion's radius, confinement refers to the magnitude of the eigenstrains, $\Phi - 1$. This diagram revealed two distinct solutions in the postbuckling region of the plate. One is a near-threshold (NT) solution that occupies a narrow area close to the flat-to-buckle instability, and second is a far-from-threshold (FFT) solution that dominates the system slightly beyond this initial buckling. While the NT solution corresponds to an extensive pattern, where the out-of-plane deformation scales with the external dimensions of the plate, the FFT solution is localized around the radius of the inclusion. This localization refers to a narrow transition layer over which the height function decays to zero exponentially. The characteristic length scale of this decay was found to depend on the system's parameters, $\ell_D \propto (\Phi - 1)^{-1/3} h^{2/3}$ [33].

Motivated by these findings, we herein investigate the interaction between two circular inclusions that buckle into a localized, FFT solution. Our investigation is carried out using two approaches, analytical and numerical. Analytically, we focus on the interaction between two inclusions that are separated far apart, i.e., $\ell - R \gg \ell_D$, where 2ℓ is the distance between the centers of the inclusions. Using a variational ansatz, we show that the leading order of this interaction energy is proportional to the interaction between the out-of-plane deformations of the two inclusions. Since the tails of these bending deformations decays exponentially in the FFT region, we conclude that the leading order of this energy behaves as $E_{\text{int}} \propto e^{-(\ell - R)/\ell_D}$. We note that the NT solution of a closely related system was recently given by Plummer and Nelson [13], who considered an array of dilational impurities in a two-dimensional crystalline membrane. Their solution revealed long-ranged interaction between the impurities and as a result, competition between several complex surface morphologies.

Numerically, we investigate the minimizers of the FvK model by the straightforward solution of its corresponding equilibrium equations. While the analytical model shows good agreement with the numerical results at large separations, significant deviations are encountered at shorter distances, $\ell - R \sim \ell_D$. In particular, we explore two different solutions within the FFT region [11,34]. One is the "up-up" scenario, where the two inclusions buckle in the same direction, and second is the "up-down" scenario, where buckling occurs in opposite directions. Three interesting results are obtained within this numerical investigation. First, the interaction energy behaves nonmonotonically in both solutions. While it increases sharply when $0 < \ell - R \ll \ell_D$, it decays to zero exponentially as in a Morse-like potential at larger distances. Second, the up-down scenario is always energetically preferable over the up-up solution. Third, while the up-up solution remains symmetric at any mutual separation, i.e., the left and right inclusions have the same amplitudes, the up-down solution develops into an asymmetric shape. The latter effect is also verified qualitatively by our gel lattice spring model (gLSM), which accounts for the complete elastodynamic behavior of polymeric gels [35–37].

The paper is organized as follows. In Sec. II we formulate the problem and derive the corresponding equilibrium equations. In Sec. III, we derive an approximate analytical solution in the case where the inclusions are separated relatively far apart (the far separation region) and show that it corresponds to an exponentially decaying interaction energy. In Sec. IV, we present our numerical investigation and compare it with the analytical solution. Last, in Sec. V, we conclude and suggest some extensions for a future research.

II. FORMULATION OF THE PROBLEM

Our system consists of an infinite plate with thickness h that contains two circular inclusions with radius R. The centers of the inclusions are located at a distance 2ℓ apart. Following the standard terminology, the region outside the inclusions is called the "matrix." The inclusions are subjected to in-plane dilative strains (swelling) compared to the matrix (see Fig. 1). This dilation is modeled by the following reference metric:

$$\bar{g}_{\alpha\beta} = h(\mathbf{r})^2 (dr^2 + r^2 d\theta^2), \quad h(\mathbf{r}) = \begin{cases} \Phi & \mathbf{r} \in \text{inclusions} \\ 1 & \mathbf{r} \in \text{matrix} \end{cases}, \tag{1}$$

where (r, θ) are polar coordinates that originate from the center of the right inclusion, $\mathbf{r}$ is a position vector to a point on the plate, and Φ is a constant that characterizes the dilation in the inclusions. In this analysis we assume that $0 < \Phi - 1 \ll 1$. The assumption that $\Phi \geqslant 1$ guarantees that the inclusions buckle into a spherical-cap-like shape [38] and the assumption that $\Phi - 1 \ll 1$ corresponds to small strain approximation. In addition, we define the Cartesian coordinates (x, y) at the center of the right inclusion, i.e., $x = r\cos\theta$ and $y = r\sin\theta$. Although polar coordinates are used in this section, the Cartesian representation will be of interest in some of our derivations. For this reason, the essential formulas in the (x, y) coordinates are summarized in Appendix A.

The final 3D configuration is given by

$$\mathbf{f}_j(r, \theta) = \left[\sqrt{\bar{g}_{rr}} r + u_r^j(r, \theta)\right]\hat{\mathbf{r}} + u_\theta^j(r, \theta)\hat{\boldsymbol{\theta}} + \zeta_j(r, \theta)\hat{\mathbf{z}}, \tag{2}$$

where hereafter the subscript or superscript $j = I_R, I_L, M$ accounts for quantities that are calculated in the right or left inclusions or the matrix, respectively. In addition, $u_r^j(r, \theta)$ and $u_\theta^j(r, \theta)$ are the respective radial and azimuthal displacements and $\zeta_j(r, \theta)$ are the height functions. The unit vectors $\hat{\mathbf{r}}$, $\hat{\boldsymbol{\theta}}$, and $\hat{\mathbf{z}}$, are oriented in the respective radial, azimuthal, and z directions and form a cylindrical coordinate system.

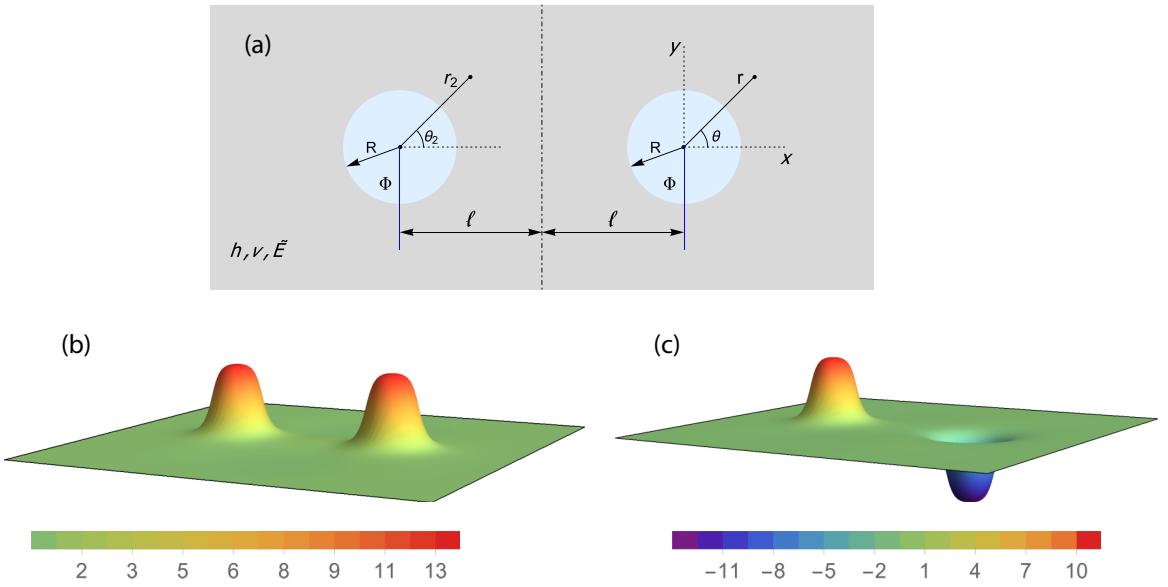

FIG. 1. Schematic overview of the system. (a) Top view. Two circular inclusions with radius R (light blue areas) are confined within an infinite plate with thickness h, Young's modulus $\tilde{E}$, and Poisson's ratio ν. The centers of the inclusions are located at a distance 2ℓ apart, and their areas are swelled by a factor Φ compared to the matrix (light gray area). The origin of the polar and the Cartesian coordinates are located at the center of the right inclusion such that the center axis is at $x = -\ell$ (dashed-dotted line). In addition, we define the polar coordinates from the center of the left inclusion (r_2, θ_2), where $r_2 = \sqrt{(2\ell)^2 + r^2 + 4\ell r \cos\theta}$. We anticipate the deformation of the plate to yield either the up-up profile, where the two inclusions buckle in the same direction (b), or up-down profile, where the two inclusions buckle in opposite directions (c). The latter panels reveal two results from our numerical simulations in Sec. IV, where $h = 1$, $R/h = 60$, $\Phi = 1.02$, $\nu = 0$, and $\ell/h = 160$. Color-bars indicate the height in units of the plate's thickness.

The total elastic energy of the system is the sum of the energies of the inclusions and the matrix, $E = E^{I_R} + E^{I_L} + E^{M}$, where each region has two contributions, one from stretching, E_s^j, and second from bending, E_b^j. Therefore, the total energy is

$$E = \sum_{j=I_R,I_L,M} \left(E_s^j + E_b^j\right), \tag{3}$$

where the stretching and bending contributions are given by

$$E_s^j = \frac{1}{2}\iint \sigma_{\alpha\beta}^j \epsilon_{\alpha\beta}^j r d\theta dr, \tag{4a}$$

$$E_b^j = \frac{1}{2}\iint M_{\alpha\beta}^j \phi_{\alpha\beta}^j r d\theta dr, \tag{4b}$$

and by the standard notation repeated indices imply summation. The integrations in Eqs. (4) are taken either over the areas of the right or left inclusions or the area of the matrix. In addition, the tensors $\sigma_{\alpha\beta}^j$ and $M_{\alpha\beta}^j$ are respectively the stresses and bending moments, and $\epsilon_{\alpha\beta}^j$ and $\phi_{\alpha\beta}^j$ are the respective strains and "bending strains."

The stresses and the bending moments are related to the strains by the linear relations, $\sigma_{\alpha\beta}^j = Y[(1-\nu)\epsilon_{\alpha\beta}^j + \nu\epsilon_{\gamma\gamma}^j\delta_{\alpha\beta}]$ and $M_{\alpha\beta}^j = B[(1-\nu)\phi_{\alpha\beta}^j + \nu\phi_{\gamma\gamma}^j\delta_{\alpha\beta}]$, where $Y = \tilde{E}h/(1-\nu^2)$ and $B = \tilde{E}h^3/[12(1-\nu^2)]$ are the respective stretching and bending moduli of the plate, ν is Poisson's ratio, and $\tilde{E}$ is the Young's modulus. In addition, the constitutive relations between the strains, as well as the bending strains and the displacements, are given by

$$\epsilon_{rr}^j = \partial_r u_r^j + \frac{1}{2}(\partial_r \zeta_j)^2,$$

$$\phi_{rr}^j = \partial_{rr}\zeta_j, \tag{5a}$$

$$\epsilon_{r\theta}^j = \frac{1}{2r}\partial_\theta u_r^j - \frac{1}{2r}u_\theta^j + \frac{1}{2}\partial_r u_\theta^j + \frac{1}{2r}\partial_r\zeta_j\partial_\theta\zeta_j,$$

$$\phi_{r\theta}^j = \partial_r\left(\frac{1}{r}\partial_\theta\zeta_j\right), \tag{5b}$$

$$\epsilon_{\theta\theta}^j = \frac{u_r^j}{r} + \frac{1}{r}\partial_\theta u_\theta^j + \frac{1}{2r^2}(\partial_\theta\zeta_j)^2,$$

$$\phi_{\theta\theta}^j = \frac{1}{r}\partial_r\zeta_j + \frac{1}{r^2}\partial_{\theta\theta}\zeta_j. \tag{5c}$$

When the system reaches equilibrium the elastic energy is extremized. Therefore, we minimize Eqs. (3) and (4) with respect to the displacements, u_r^j, u_θ^j, and ζ_j, and obtain the following equilibrium equations:

$$\partial_r\left(r\sigma_{rr}^j\right) - \sigma_{\theta\theta}^j + \partial_\theta\sigma_{r\theta}^j = 0, \tag{6a}$$

$$\partial_r\left(r\sigma_{r\theta}^j\right) + \sigma_{r\theta}^j + \partial_\theta\sigma_{\theta\theta}^j = 0, \tag{6b}$$

$$B\Delta^2\zeta_j - \sigma_{\alpha\beta}^j\phi_{\alpha\beta}^j = 0, \tag{6c}$$

where $\Delta = \partial_{rr} + \frac{1}{r}\partial_r + \frac{1}{r^2}\partial_{\theta\theta}$ is the Laplace operator. Equations (6a), (6b), and (6c) correspond to the force balance in the radial, azimuthal, and normal directions, respectively. Closure

is obtained once these equations are supplemented with the following boundary conditions on the edges of the inclusions:

$$\text{continuity of the surface:} \quad \mathbf{f}_i(r_i,\theta) = \mathbf{f}_M(r_i,\theta), \tag{7a}$$

$$\partial_r \zeta_i(r_i,\theta) = \partial_r \zeta_M(r_i,\theta), \tag{7b}$$

$$\text{continuity of momentum:} \quad \sigma^i_{r\mu}(r_i,\theta) = \sigma^M_{r\mu}(r_i,\theta), \quad (\mu = r,\theta,z), \tag{7c}$$

$$M^i_{rr}(r_i,\theta) = M^M_{rr}(r_i,\theta), \tag{7d}$$

where $i = I_R, I_L$ and the radius r_i points either to the edge of the right or left inclusion. In addition, $\sigma^j_{rz} = \partial_r(rM^j_{rr}) - M^j_{\theta\theta} + 2\partial_\theta M^j_{r\theta} - r\sigma^j_{rr}\partial_r\zeta_j - \sigma^j_{r\theta}\partial_\theta\zeta_j$ is the normal stress at a cross section, and we assume that the deformation of the plate decays to zero at infinity, i.e., the stresses and the bending moments vanish all together when $r \to \infty$.

Finally, we define the energy of interaction by

$$E_{\text{int}} \equiv E - E_\infty, \tag{8}$$

where E is given by Eqs. (3) and (4) and $E_\infty = E(\ell \to \infty)$. The latter definition bears the assumption that the interaction between the inclusions decay to zero as ℓ increases. In the limit $\ell \to \infty$ we expect that $E(\ell \to \infty) = 2E_{1i}$, where E_{1i} is the energy of a single inclusion, with radius R and swelling factor Φ, in an infinite plate with thickness h.

Although Eqs. (6) and (7) provide the complete set of equilibrium equations, we add one modification that will be helpful in the next section. Following Ref. [24, p. 52], the force balance equations in the radial and the azimuthal directions, Eqs. (6a) and (6b), are automatically satisfied when

$$\begin{aligned} \sigma^j_{rr} &= \frac{1}{r}\partial_r U^j + \frac{1}{r^2}\partial_{\theta\theta} U^j, \\ \sigma^j_{r\theta} &= -\partial_r\left(\frac{1}{r}\partial_\theta U^j\right), \\ \sigma^j_{\theta\theta} &= \partial_{rr} U^j, \end{aligned} \tag{9}$$

where $U^j(r,\theta)$ are the so-called Airy's stress functions. At equilibrium, these functions satisfy the compatibility conditions,

$$\Delta^2 U^j = -\tilde{E}h\left[\phi^j_{rr}\phi^j_{\theta\theta} - \left(\phi^j_{r\theta}\right)^2\right], \tag{10}$$

where the $\phi^j_{\alpha\beta}$ are given in Eqs. (5). The right-hand side of Eqs. (10) are proportional to the Gaussian curvature on the plate and depend solely on the height functions $\zeta_j(r,\theta)$.

In summary, given the swelling Φ, and the stretching and bending moduli, Y and B, we determine the final deformation of the plate from the solution of the equilibrium equations, Eqs. (6), and the boundary conditions, Eqs. (7). The solution of the latter equations is equivalent to the solution of Eqs. (6c) and (10) under the same set of boundary conditions. In these equations, the stresses are related to the strains by Hooke's law and the strain-displacements relations are given by Eqs. (5). In general, the nonlinearity of the equilibrium equations implies that the solution is not unique. Among the set of possible solutions, only the one with the lowest energy is realized experimentally. While the total energy of the minimizer, E, is determined from Eqs. (3) and (4), the interaction energy, E_{int}, is determined from Eq. (8).

In general, the complexity of our equations does not allow a tractable analytical treatment. For this reason, their straightforward solution, i.e., without any simplifications, is obtained numerically in Sec. IV. A further analytical treatment is considered in the next section under a certain set of simplifying assumptions.

III. APPROXIMATED ANALYTICAL SOLUTION IN THE FAR SEPARATION REGION

This section is divided into two parts. While in the first part, we introduce our set of simplifying assumptions, in the second part, we utilize these assumptions to derive the approximated solution of the problem. We show that when the separation between the two inclusions is large, the interaction energy decays to zero exponentially, i.e., $E_{\text{int}} \propto e^{-(\ell-R)/\ell_D}$, where ℓ_D characterizes the localization of the elastic pattern.

A. Assumptions

The approximated solution is derived under the following assumptions. First, the deformation of the plate is localized around the areas of the inclusions. In Ref. [32], we showed that a plate with a single inclusion localizes the elastic deformation given that the bendability, h/R, is small enough, and the confinement is set above a certain threshold, $\Phi - 1 > \epsilon$. This localized state was referred to as the FFT solution. Second, the mutual distance between the inclusions is large compared with the elastic relaxation of the buckled profile, $\ell - R \gg \ell_D$.

Third, we assume that the final configuration is symmetric around the middle axis $x = -\ell$ [dashed-dotted line in Fig. 1(a)]. This assumption will allow us to consider only one-half of the plate, say, $x \geqslant -\ell$, while setting symmetric boundary conditions at $x = -\ell$,

$$u^M_x(-\ell, y) = \sigma^M_{xy}(-\ell, y) = 0. \tag{11}$$

In the latter equation, $u^M_x(x,y)$ and $\sigma^M_{xy}(x,y)$ are the horizontal displacement and shear stress in the Cartesian representation, see Appendix A. In addition, since we are now dealing with only one inclusion, we will simplify our notation and use the subscript or superscript $j = I, M$ (instead of $j = I_R, I_L, M$) to denote quantities that are related to the right inclusion or the matrix to the right of the axis of symmetry.

Fourth, we assume that each inclusion buckles into an axisymmetric shape up to small asymmetric corrections that diminish as the mutual separation increases. Considering the symmetry around $x = -\ell$, this assumption implies that

$$\zeta_j(r,\theta) \to \zeta_j(r) \pm \zeta_M(r_2), \tag{12}$$

where $\zeta_j(r)$ is an axisymmetric function that depends solely on the radial coordinate and $\zeta_M(r_2)$ is the contribution from the tail of the left inclusion [see Fig. 1(a) for the definition of r_2]. The latter contribution aims at satisfying the boundary conditions, Eq. (11), where plus and minus correspond to up-up and up-down scenarios, respectively; see Figs. 1(b) and 1(c).

Fifth, we assume that $\zeta_j(r)$ are given by

$$\zeta_I(r) = A[1-(r/R)^{\alpha}], \tag{13a}$$

$$\zeta_M(r) = -A[1-(r/R)^{-\alpha}], \tag{13b}$$

where A and α are two variational constants that are yet to be determined by minimization of the total energy. In Ref. [32], this ansatz presented good agreement with the numerical solution of the FFT profile. This chosen function is motivated by the fact that thin sheets tend to accommodate the Gaussian curvature of the reference metric in order to minimize their stretching energy [39]. Although the reference metric, Eq. (1), prescribes zero Gaussian curvature in both regions, the inclusions and the matrix, it contains a discontinuity on the edge of the inclusion. Therefore, we expect the morphology of each region to converge into a flat state up to narrow transition layers accommodated around the inclusions' edges. This behavior is obtained in Eq. (13) when $\alpha \gg 1$. In this limit, we have that $(r/R)^{\pm\alpha} \simeq e^{\pm\frac{r-R}{\ell_D}}$, where $\ell_D = R/\alpha$ is the length of the transition layer [40].

Last, since the tail of the left inclusion is expected to decay exponentially, $\zeta_M(r_2) \propto e^{-\frac{r_2-R}{\ell_D}}$, we neglect it in the leading-order approximation, i.e., we assume that $\zeta_j(r,\theta) \simeq \zeta_j(r)$. Note that with this assumption, the up-up and up-down scenarios become indistinguishable. Note also that although this ansatz is independent on ℓ, this parameter is not absent from the analysis of the leading-order approximation. It yet plays a role in the boundary conditions imposed on the in-plane equations, i.e., when $A = 0$, the solution must converge to the one expected from a flat plate with two circular inclusions [17].

Utilizing the above assumptions, our goal in the next section is to show that the interaction energy of the system, $E_{\rm int}$, vanishes identically in the leading-order approximation. Consequently, the first nontrivial contribution to $E_{\rm int}$ must be proportional to subleading-order terms that are akin to the deformation of the left inclusion, $\zeta_M(r_2)$. Since the latter corrections decays exponentially in the FFT region, we would expect the first nontrivial contribution to $E_{\rm int}$ to decay exponentially as well.

B. Solution to leading order

This section is divided into three parts. First, given the above assumptions, we find an exact solution to Eq. (10). Second, we utilize this solution to calculate the total energy of the system, $E(A,\alpha)$ and to determine the elastic shape, i.e., the amplitude, A, and the length of transition layer, ℓ_D. Third, we discuss the main differences between this FFT solution and the solution of the flat configuration.

1. Solution to Eqs. (10)

In this section, we derive the solution of Eqs. (10) under the set of simplifying assumptions made in Sec. III A. These equations recover the problem of plane stress in linear elasticity where the right-hand side of the equations, which depends solely on the height function, takes the role of external body forces. For this reason, we adopt the complex formulation of planar elasticity [41–43] and extend it to include corrections due to the "external forces." As discussed in the latter references, this technique is adequate to deal with nontrivial geometrical boundaries that include both the circular interface of the inclusion, $r = R$, and the vertical line of symmetry, $x = -\ell$ [44].

Following the derivations in Appendix B, it can be shown that the solution of Eqs. (10) reads,

$$\frac{\tilde{E}t}{1+\nu}\left(u_r^j + iu_\theta^j\right)e^{i\theta} = \frac{3-\nu}{1+\nu}\phi_j(z) - (z+\ell)\overline{\phi_j'(z)} - \overline{\psi_j(z)} + \frac{e^{i\theta}}{1+\nu}\left(r\partial_{rr}U_p^j - \nu\partial_r U_p^j\right), \tag{14a}$$

$$\sigma_{\theta\theta}^j + \sigma_{rr}^j = 2[\phi_j'(z) + \overline{\phi_j'(z)}] + \partial_{rr}U_p^j + \frac{1}{r}\partial_r U_p^j, \tag{14b}$$

$$\sigma_{\theta\theta}^j - \sigma_{rr}^j + 2i\sigma_{r\theta}^j = 2[(\bar{z}+\ell)\phi_j''(z) + \psi_j'(z)]e^{2i\theta} + \partial_{rr}U_p^j - \frac{1}{r}\partial_r U_p^j, \tag{14c}$$

where $z = x + iy = re^{i\theta}$ is a complex variable ($i = \sqrt{-1}$), the overbar denotes the complex conjugate, and prime $(\,)'$ indicates a derivative with respect to z. In addition, the functions $U_p^j(r)$ are the particular solutions to the Airy's stress functions, and $\phi_j(z)$ and $\psi_j(z)$ are arbitrary complex potentials. Note that Eqs. (14) hold only for the case of an axisymmetric height function; their general form is given in Appendix B.

It is left to determine $\phi_j(z)$, $\psi_j(z)$, and $U_p^j(r)$ that satisfy the appropriate set of boundary conditions, i.e., Eqs. (7a) and (7c) in the r and θ directions and Eqs. (11) on the axis of symmetry. Since the derivation of these unknown functions is cumbersome the details are presented in Appendix C. The solutions read,

$$\phi_I(z) = \left[-\frac{\sigma_o}{2} + \frac{\tilde{E}h\,\alpha^3 A^2}{8(\alpha^2-1)R^2}\right]z, \tag{15a}$$

$$\psi_I(z) = \frac{\sigma_o \ell}{2}\left[1 - \frac{R^2/\ell^2}{1+z/(2\ell)}\right] - \frac{\tilde{E}h\,\ell\alpha^3 A^2}{8(\alpha^2-1)R^2}\left\{1 - \frac{(\alpha^2-1)R^2}{\alpha^2\ell^2[1+z/(2\ell)]}\right\}, \tag{15b}$$

$$\phi_M(z) = 0, \tag{15c}$$

$$\psi_M(z) = -2\left(\sigma_o R^2 - \frac{\tilde{E}h}{4}\alpha A^2\right)\frac{z+\ell}{z(z+2\ell)}, \tag{15d}$$

and

$$U_p^I(r) = -\frac{\tilde{E}hA^2}{16(\alpha-1)}\left(\frac{r}{R}\right)^{2\alpha},$$

$$U_p^M(r) = \frac{\tilde{E}hA^2}{16(\alpha+1)}\left(\frac{r}{R}\right)^{-2\alpha}. \tag{16}$$

where $\sigma_o = \tilde{E}h(\Phi-1)/2$. Indeed, Eqs. (15) depend on the parameter ℓ although our ansatz, $\zeta_j(r,\theta) \simeq \zeta_j(r)$, is independent of this parameter. When $A = 0$, this solution converges to the exact solution of a flat plate with two circular inclusions [17].

2. Energy, amplitude, and transition layer

Using Eqs. (15) and (16), we can calculate the elastic energy as a function of the variational parameters, $E(A,\alpha)$.

This calculation is somewhat simplified given our set of assumptions. Indeed, following the derivations in Appendix D, it can be shown that Eqs. (3) and (4) are equivalent to the calculation of the following integral:

$$\text{leading order:}\quad E = (1-\Phi)R^2\int_0^{2\pi}\sigma_{rr}^I(R,\theta)d\theta + \frac{1}{2}\sum_{j=I,M}\iint\sigma_{rr}^j(\partial_r\zeta_j)^2 rd\theta dr + \sum_{j=I,M}E_b^j, \tag{17}$$

where the first two terms are obtained from the stretching energy, and the third term is the bending contribution, see Eq. (4b). We add three comments regarding Eq. (17). First, when $\zeta_j(r)=0$ the last two terms vanish identically, and the energy of the flat state is obtained by a line integral over the boundary of the right inclusion. Second, the integrals in Eq. (17) refer either to the area of the right inclusion or the area of the matrix to the right of the axis of symmetry, $x=-\ell$. In addition, we keep in mind that terms of order $(R/2\ell)^\alpha$ are neglected in our leading-order approximation. Third, since the height functions, $\zeta_j(r)$, are already given by the ansatz, Eqs. (13), we can perform the explicit integration once we determine the radial stresses, σ_{rr}^j, in both regions. These stresses are obtained from Eqs. (14)–(16).

Integrating Eq. (17) gives the following result:

$$E = 2E_f\left[1-\frac{\alpha(2\alpha+1)A^2}{2(\alpha+1)(\Phi-1)R^2} + \frac{\alpha^4(4\alpha+1)A^4}{4(\alpha+1)(4\alpha^2-1)(\Phi-1)^2R^4}\right] + \frac{2\pi BA^2\alpha^5}{R^2(\alpha^2-1)}, \tag{18}$$

where we defined the energy of the flat configuration ($A=0$) by $2E_f=\pi\tilde{E}hR^2(\Phi-1)^2$. This flat-state energy is equal to twice the energy of a single inclusion in an infinite plate. Therefore, it recovers the well-known result that the interaction energy between two flat and circular inclusions vanish identically [2,45].

Evidently, $E_{\text{int}}=0$ also in the leading order of our buckled solution. This is because Eq. (18) is independent on the parameter ℓ. This result imply that the inclusions do not "attract" or "repel" each other in both the flat and the FFT solutions. Nonetheless, while the solution to the flat state is exact and holds for any mutual separation $R/2\ell$, the FFT solution holds only to leading order under the set of assumptions made in Sec. III A. In particular, since the subleading correction of this expansion is proportional to the bending deformation of the left inclusion, $\zeta_M\propto e^{-\frac{r_2-R}{\ell_D}}$, we would expect the same exponential decay in E_{int}. Indeed, as we further discuss in Sec. IV, numerical investigation of the problem reveals nonzero interaction when the transition layers of the two inclusions coalesce, $\ell-R\sim\ell_D$.

To complete the calculation we need to determine the variational parameters A and α as a function of the system's parameters. Following the analysis in Ref. [32] we expand Eq. (18) in powers of $1/\alpha$ assuming that $A\propto\alpha^{-1/2}$. This gives

$$E_{\text{FFT}} = 2E_f\left[1-\frac{\alpha A^2}{2(\Phi-1)R^2}\right]^2 + \frac{\pi}{2}\tilde{E}hR^2(\Phi-1)\left[1-\frac{3\alpha A^2}{8(\Phi-1)R^2}\right]\frac{A^2}{R^2} + 2\pi B\alpha^3\frac{A^2}{R^2}, \tag{19}$$

where the first and second terms on the right-hand side are respectively the leading and subleading orders of the stretching energy, and the third term is the bending energy. Minimizing the leading order of this energy with respect to A gives $A/R=\sqrt{2(\Phi-1)/\alpha}$. Substituting the latter amplitude back in the energy and minimizing it with respect to α gives the required solution,

$$\alpha = (3/8)^{1/3}(1-\nu^2)^{1/3}(\Phi-1)^{1/3}(R/h)^{2/3}. \tag{20}$$

Equation (20) coincides with our solution in Ref. [32] for the case of a single inclusion [see Eq. (19) in that paper]. Using Eq. (20) we find that the length of the transition layer, $\ell_D=R/\alpha$, the amplitude, and the energy, Eq. (19), are given by

$$\ell_D = (8/3)^{1/3}(1-\nu^2)^{-1/3}(\Phi-1)^{-1/3}(h/R)^{2/3}R, \tag{21a}$$

$$A/R = \left[2(\Phi-1)\frac{\ell_D}{R}\right]^{1/2}, \tag{21b}$$

$$E_{\text{FFT}}/2E_f = \frac{3\ell_D}{8R}, \tag{21c}$$

These results complete our approximated analytical solution. In summary, for a given Φ, R, ℓ, and the physical parameters ν and $\tilde{E}$, the height function is given by Eqs. (12) and (13), where A and α are determined from Eqs. (20) and (21b). In addition, the in-plane displacements are obtained from Eqs. (14)–(16). We note that the limits of this solution with respect to the small slope approximation are discussed in Ref. [32].

3. *Stress distribution and relative separation—Comparison between the flat and FFT solutions*

In this section we further characterize the interaction between the inclusions and calculate (i) the stresses on the edge of the right inclusion, $\sigma_{\alpha\beta}^j(R,\theta)$, and (ii) the relative distance between the inclusions' centers, i.e., $\Delta_c\equiv 2[\mathbf{f}(0,0)-\mathbf{f}(-\ell,0)]\cdot\hat{\mathbf{x}}$. Aiming for comparison, these FFT quantities will be compared with their counterparts in the flat configuration.

To calculate the stresses and the relative separation in the FFT solution, we substitute Eqs. (15) and (16) in Eqs. (14) and expand the resulting expressions to leading order in powers of $1/\alpha$. Using our FFT solution, Eqs. (20) and (21b), we obtain

FFT (leading order):

$$\sigma_{rr}^j(R,\theta)/\sigma_o = -\frac{\ell_D}{2R}, \tag{22a}$$

$$\sigma_{r\theta}^j(R,\theta)/\sigma_o = 0, \tag{22b}$$

$$\sigma_{\theta\theta}^j(R,\theta)/\sigma_o = \pm 1, \tag{22c}$$

$$\Delta_c/2\ell = 1, \tag{22d}$$

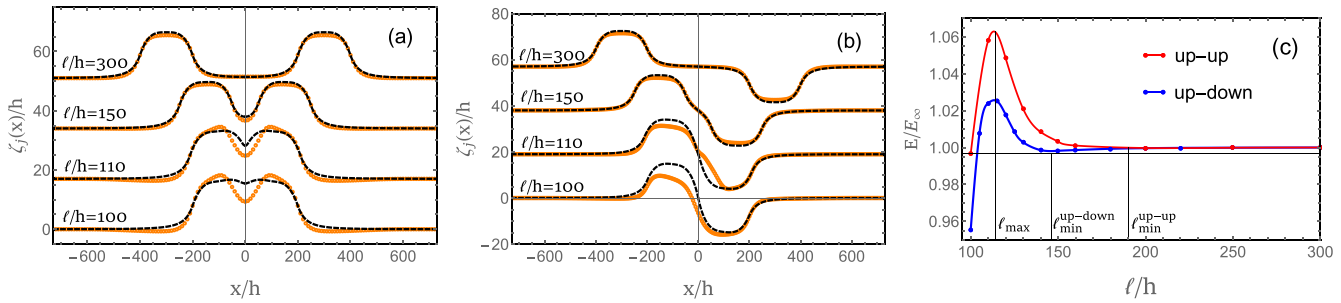

FIG. 2. Height profiles and total energy as a function of ℓ/h ($R/h = 100$). In panels (a) and (b) we plot the cross sections of the height profile for several values of ℓ/h. In both panels, the dashed black line corresponds to our ansatz, Eqs. (12) and (13), where the variational parameters are determined from Eqs. (20) and (21b), and orange circles correspond to the numerical solution. The cross sections are considered at $y = 0$, where the origin is placed at the center point between the inclusions. While panel (a) corresponds to the up-up solution, panel (b) corresponds to the up-down solution. The ansatz based solution agrees nicely (up to 10% difference) with the numerical data for large values of ℓ/h but breaks down at smaller separations. In addition, note that while the up-up solution maintains the profile's symmetry even at small separations, the up-down profile becomes asymmetric. (c) The energy, Eqs. (3) and (4), as a function of ℓ/h. The energy of the up-up and up-down solutions are given by the dotted solid red and dotted solid blue lines, respectively. Dots on the corresponding curves represent the numerical data, and the solid lines are their interpolations. The up-down solution is always energetically preferable over the up-up scenario. In addition, both profiles are nonmonotonic functions of ℓ/h. Short-range attraction is observed between $R < \ell < \ell_{\max}$, where $\ell_{\max}/h \simeq 114$. Short-range repulsion is observed for $\ell_{\max} < \ell < \ell^{i}_{\min}$, where $\ell^{\text{up-down}}_{\min}/h \simeq 146$ and $\ell^{\text{up-up}}_{\min}/h \simeq 190$. The minimum of the up-up is shallower compared to the up-down solution and is hardly seen in the figure. When $\ell > \ell^{i}_{\min}$, both energies present long-range attraction. Asymptotically, the numerical energy converges to $E_\infty/(\tilde{E}h^3) \simeq 0.329$, which is comparable with our analytical prediction in Eq. (21c), $E_{\text{FFT}}/(\tilde{E}h^3) \simeq 0.351$.

where $\sigma_o = \tilde{E}h(\Phi - 1)/2$. While the radial and the shear stresses are continuous across the boundary of the inclusion, as dictated by the boundary conditions Eqs. (7c), the azimuthal stresses are discontinuous, i.e., they are negative in the inclusion and positive in the matrix.

To compute the counterparts of Eqs. (22) in the flat configuration we set $A = 0$ in the potentials, Eqs. (15), and take $U^j_p(r) = 0$. This gives on substitution into Eqs. (14),

Flat (exact):

$$\sigma^j_{rr}(R,\theta)/\sigma_o = -1 - \frac{R^2}{\bar{r}_2^2}\left(1 - \frac{8\ell^2}{\bar{r}_2^2}\sin^2\theta\right), \tag{23a}$$

$$\sigma^j_{r\theta}(R,\theta)/\sigma_o = \frac{4R\ell}{\bar{r}_2^2}\left(1 - \frac{4\ell^2 + 2R\ell\cos\theta}{\bar{r}_2^2}\right)\sin\theta, \tag{23b}$$

$$\sigma^j_{\theta\theta}(R,\theta)/\sigma_o = \pm 1 + \frac{R^2}{\bar{r}_2^2}\left(1 - \frac{8\ell^2}{\bar{r}_2^2}\sin^2\theta\right), \tag{23c}$$

$$\Delta_c/2\ell = 1 + \frac{(1+\nu)(\Phi-1)R^2}{4\ell^2}, \tag{23d}$$

where $\bar{r}_2 = \sqrt{(2\ell)^2 + R^2 + 4R\ell\cos\theta}$ is the radial coordinate from the center of the left inclusion to the edge of the right inclusion.

Comparing Eqs. (22) and (23) reveals an essential difference between the flat and FFT solutions. While the former equations are independent on ℓ, the latter equations do depend on it. Although the inclusions do not interact energetically in both solutions, in the flat state the inclusions do "sense" each other due to the distortions in the stress field. This complete screening in the FFT solution is a signature of the exponential decay of the interaction energy, as we further show numerically in the next section.

IV. NUMERICAL INVESTIGATION IN CLOSE AND FAR SEPARATION REGIONS

This section is devoted to numerical investigation of the problem. Our numerical scheme, for the solution of the FvK equations, follows the analysis in Refs. [34,46] but includes some modifications that account for the boundary conditions on the plate's edges; the details of the algorithm are given in Appendix E. Our simulation box consists of a square, two-dimensional, grid of size $L\times L$, where $L/h = 2500$ and $h = 1$. The physical constants of the plate are $\tilde{E} = 1$ and $\nu = 0$. In addition, the inclusions' radii and the relative separations are varied in the range $R/h \in [60, 100]$ and $\ell \in [R, R + 7\ell_D]$, and the swelling factor is set at a constant value, $\Phi - 1 = 0.01$. The numerical scheme converges either to the up-up solution, Fig. 1(b), or the up-down solution, Fig. 1(c), depending on the parity prescribed by the initial guess.

In Figs. 2(a) and 2(b) we compare the numerical height functions with the analytical solution when $R/h = 100$ and $\ell = \{100, 110, 150, 300\}$, such that $(\ell - R)/\ell_D \simeq \{0, 0.3, 1.6, 6.6\}$ ($\ell_D/h \simeq 29.8$). The analytical solution is given by Eqs. (12) and (13), where α and A are obtained from Eqs. (20) and (21b). In both the up-up and up-down cases, the variational ansatz agrees nicely with the numerical solution for large separations, $\ell/h = \{150, 300\}$, but breaks down when $\ell/h = \{100, 110\}$. The total energies of these shapes, Eqs. (3) and (4), are presented in Fig. 2(c). Evidently, the up-down solution has slightly lower energy compared with the up-up case. While the energies of the two solutions converge to $E_\infty/(\tilde{E}h^3) \simeq 0.329$ when $\ell/h \gtrsim 160$, they deviate as their mutual distance decreases. The latter asymptotic energy is comparable with the analytical approximation, which gives $E_{\text{FFT}}/(\tilde{E}h^3) \simeq 0.351$ [see Eq. (21c)].

As reported in Ref. [34], the close separation region presents nonmonotonic behavior. When $R < \ell < \ell_{\max}$ we find

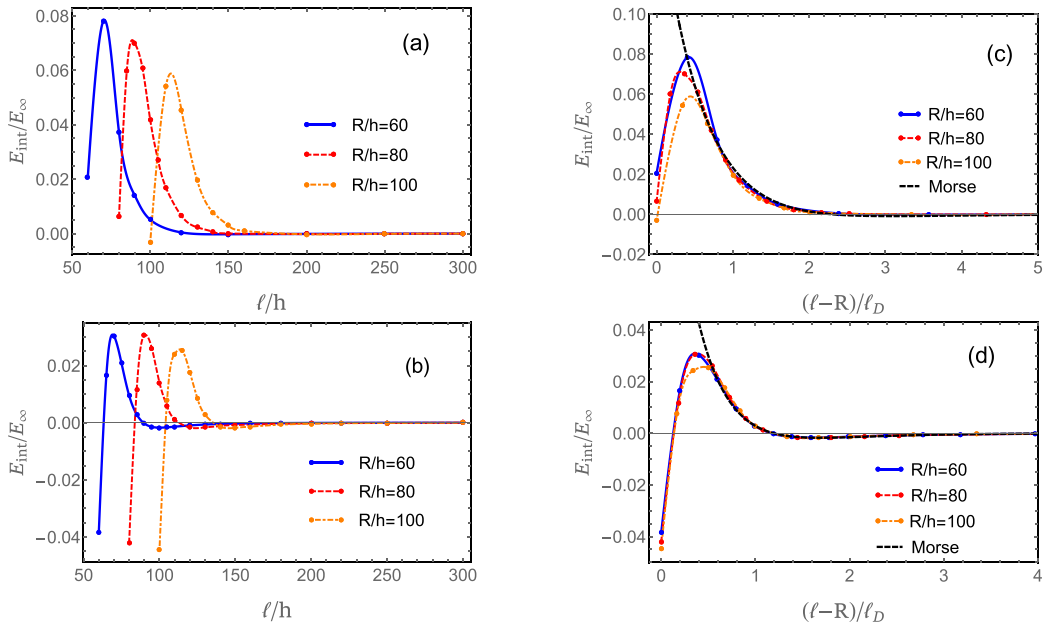

FIG. 3. Numerical investigation of the interaction energy. In panels (a) and (b) we plot $E_{\rm int}/E_\infty$ as a function of ℓ/h for several $R/h = \{60, 80, 100\}$ (solid blue, dashed red, dashed-dotted orange). Dots on the corresponding curves represent the numerical data. While panel (a) corresponds to the up-up solution, panel (b) corresponds to the up-down solution. In both cases the tail of the data collapse on a single master curve once we redefine the x axis, $\ell/h \to (\ell - R)/\ell_D$. The collapse of the data for the up-up and up-down cases, respectively, are presented in panels (c) and (d). The master curve is approximated by the Morse potential (dashed black), $V(x) = a_1(1 - e^{-a_2(x-a_3)})^2 - a_1$, where $x = (\ell - R)/\ell_D$, and a_i $(i = 1 \cdots 3)$ are the fitting constants. For the up-up we find $\{a_1, a_2, a_3\} = \{9.6\times10^{-4}, 0.85, 3.09\}$ and for the up-down $\{a_1, a_2, a_3\} = \{1.7\times10^{-3}, 1.38, 1.69\}$.

short-ranged attraction, between $\ell_{\rm max} \leqslant \ell \leqslant \ell^i_{\rm min}$ (i = up-up, up-down) short-range repulsion, and when $\ell \gtrsim \ell^i_{\rm min}$ long-range attraction. While $\ell_{\rm max}$ approximately obtains the same value for both the up-up and up-down solutions, $\ell^i_{\rm min}$ depends on the given scenario. Obviously, the analytical analysis in Sec. III is applicable only at the tails of these profiles.

Considering our analytical investigation, we anticipate large deviations from E_∞ when the transition layers of the inclusions coalesce, i.e., the distance between the closest edges of the inclusions and the center line, $x = -\ell$, is approximately of order ℓ_D. To check this conjecture we plot in Figs. 3(a) and 3(b) the interaction energies, Eq. (8), of the up-up and up-down solutions for several values of $R/h = \{60, 80, 100\}$. Then, in Figs. 3(c) and 3(d) we redefine the x axis such that it measures the relative separation in units of ℓ_D, i.e., $\ell/h \to (\ell - R)/\ell_D$. Indeed, we find that with this redefinition the tails of all the data sets collapse on the same master curve, which fit well with the Morse potentials. While the minimum of these potentials are located at $(\ell^{\text{up-up}}_{\rm min} - R)/\ell_D \simeq 3.09$ and $(\ell^{\text{up-down}}_{\rm min} - R)/\ell_D \simeq 1.69$, the maximum is obtained at $(\ell_{\rm max} - R)/\ell_D \simeq 0.4$ and is approximately independent on the given solution. Nonetheless, the close separation region, $(\ell_{\rm max} - R)/\ell_D \lesssim 0.4$, does not present the same universal behavior as the potentials' tails.

Symmetry breaking in the up-down solution

An interesting result that appears in our numerical investigation is shown in Fig. 2(b): The height function of the up-down solution becomes asymmetric at very small separations. To quantify this effect, we first define the respective maximum and minimum amplitudes on the plate as $A_{\rm max} = \max\{|\zeta_{I_L}(-\ell, 0)|, |\zeta_{I_R}(\ell, 0)|\}$ and $A_{\rm min} = \min\{|\zeta_{I_L}(-\ell, 0)|, |\zeta_{I_R}(\ell, 0)|\}$. Then, we plot the evolution of $A_{\rm max} - A_{\rm min}$ as a function of the normalized mutual separation, $(\ell - R)/\ell_D$ for several values of R/h, as shown in Fig. 4. Similarly to our previous observations, we find that all

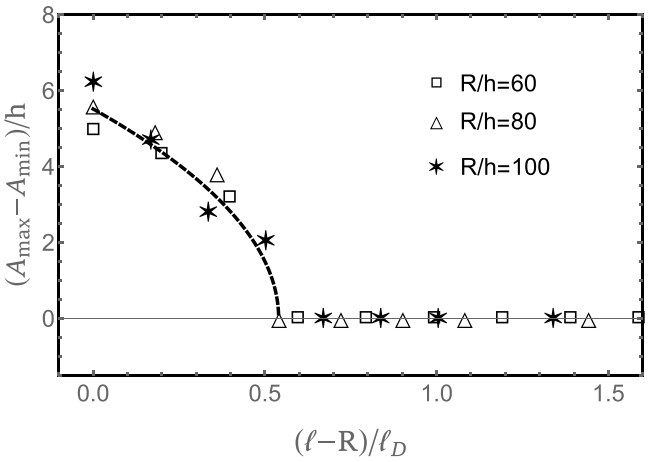

FIG. 4. Symmetry breaking in the up-down solution. The difference between the maximum and minimum amplitudes on the plate, $A_{\rm max} - A_{\rm min}$, is plotted as a function of $(\ell - R)/\ell_D$ for several values of R/h. Approximately, all data sets present the same behavior. Above $(\ell - R)/\ell_D \simeq 0.54$ the profile is symmetric and the amplitude difference is zero. Below this critical value, the difference between the amplitudes growth as $(A_{\rm max} - A_{\rm min})/h \propto [0.54 - (\ell - R)/\ell_D]^{0.5}$ (dashed line).

the data collapse on the same curve. While at $(\ell - R)/\ell_D \gtrsim 0.54$ the profile is completely symmetric and $A_{\max} = A_{\min}$, at $(\ell - R)/\ell_D \lesssim 0.54$ the profile becomes asymmetric and the difference between the maximum and minimum amplitudes approximately follows the line $(A_{\max} - A_{\min})/h \propto [0.54 - (\ell - R)/\ell_D]^{0.5}$.

To verify that this effect is not an artifact of our numerical method, we first verify that the breaking of symmetry occurs randomly either in the left or the right inclusions. We provided the initial setup with a small and random perturbation, i.e., the initial height function consisted of our ansatz Eqs. (12) and (13), and a random perturbation over the areas of the inclusions. Indeed, when we ran the simulations several times given the same system's parameters ($\Phi = 1.01$, $R/h = 60$, and $\ell/h = 70$), the maximum amplitude, $A_{\max}$, was randomly obtained either in the left or right inclusions.

Second, we verified that this symmetry breaking is not a simulation size effect. One way to estimate the accuracy of these simulations is, for example, to compare the numerical solution with the theoretical prediction in the far separation region. We keep in mind that this is only a rough estimation because the analytical profile is by itself not the exact solution. Following our numerical example, i.e., $\nu = 0$ and $\Phi = 1.01$, we find that when $R/h = 100$ and the separation is $\ell/h = 300$, the maximum numerical amplitude deviates from the analytical solution, Eq. (21b), by approximately 7%. A similar deviation is obtained when $R/h = 60$ (∼5%). Therefore, we conclude that spatial patterns with a characteristic size that is smaller than $\sim 0.1 A_{\max}$ are below the accuracy of our simulations. Following the typical examples in Fig. 2(b) where $\ell/h = 100$, we find that while the maximum height of the inclusion is $A_{\max}/h \simeq 15$, the difference between the maximum and minimum amplitudes is $A_{\max} - A_{\min} \simeq 5$. Therefore, $A_{\max} - A_{\min} \simeq 0.3 A_{\max}$ is much larger than our approximated accuracy criterion, and the symmetry breaking is not a simulation size effect.

Third, we verified that the numerical discretization of the plate is sufficiently dense to support the strong nonlinearity of the resulting pattern. Since the distance between consecutive grid points in our simulations is equivalent to the plate's thickness, $h = 1$, we must require, at least, that that the maximum spatial derivative between two consecutive points is less than one. This requirement is safely satisfied in all of our simulations. Furthermore, we identified the regions on the plate with the largest gradients in the far separation region, where we obtained good fit with the analytical solution and compared them with their counterparts in the close separation region. We found that in both cases, the density of the numerical grid is almost identical and therefore can support the largest deformation of the elastic structure.

Fourth, we investigated the symmetry breaking qualitatively using our gLSM. These simulations are based on the finite-element method and account for the complete elastodynamic behavior of polymer gels. Applied to this study, the simulation essentially mimics an experimental procedure in which gel is immersed in a thermal liquid bath. (See Refs. [36,37] for further details on this model.) Recently, we showed that these simulations adequately describe the deformation of thin elastic plates, even in the presence of localized deformations [32,47].

We simulate a single layer of gel having the dimensions $79 \times 79 \times 1$, i.e., the length and the width are equal and the thickness is of unit length. In addition, we prescribe two similar squared inclusions, $7 \times 7 \times 1$, that are separated a distance of $2\ell/h$ apart. Following Ref. [37], in this model, the network within the inclusions encompasses loops that fold and unfold as a function of the external temperature. The folding and unfolding of these loops effectively mimics the eigenstrain within the inclusion. The relation among the number of loops, the temperature, and the amount of swelling is given in Ref. [37]. We consider two mutual separations. One where the inclusions are very close, $2\ell/h = 1$, and a second where they are far apart, $2\ell/h = 33$ [see Fig. 5(a)]. For each respective separation, the system is simulated twice, once for the up-up scenario and second for the up-down case. The results of these simulations are presented in Figs. 5(b)–5(e). Indeed, the same symmetry breaking that we encountered in the FvK model appears in the gLSM. While both the up-up and up-down solutions preserve the even and odd symmetry at the large separation, Figs. 5(c) and 5(e), only the up-up scenario remains symmetric at the shorter distance [compare Figs. 5(b) and 5(d)]. Since these simulations account for nonlinear corrections in the elasticity of the gel, they essentially demonstrate that a weak nonlinearity does not overwhelm the symmetry breaking effect.

V. CONCLUSIONS

In this paper we investigated the elastic interaction between two circular inclusions in an infinite plate. We tackled the problem both analytically, Sec. III, and numerically, Sec. IV. Analytically, we utilized the assumptions in Sec. III A to investigate the limit, $\ell - R \gg \ell_D$. In this limit we showed that the energy of interaction vanishes identically to leading order, i.e., when we neglected terms of order $\zeta_M(r_2) \propto e^{-(r_2 - R)/\ell_D}$. Therefore, we concluded without explicit calculation that the first nonzero correction to the interaction energy must decay exponentially. Nonetheless, the leading-order solution provided us with a Debye-like length scale, ℓ_D, that characterizes both the decay in the elastic pattern of each inclusion and the region in which strong interaction dominates the system.

While the analytical investigation is concerned with the far separation limit, the numerical solution scanned a much wider region of the parameter space. We found good fit between the analytical predictions and the numerics when $(\ell - R) \gtrsim \ell_D$. Indeed, the height profiles at large separations, Figs. 2(a) and 2(b), and the collapse of the interaction energies' tails, Figs. 3, rely on our analytical predictions, either by the variational ansatz solution, Eqs. (13), (20), and (21b), or by the characteristic length scale, ℓ_D, Eq. (21a). Nonetheless, when $\ell - R \sim \ell_D$ the analytical analysis broke down. In particular, the following three observations were predicted only numerically. First, the up-down solution is energetically preferable over the up-up solution. Second, the interaction energy has nonmonotonic shape, i.e., it accommodates short-range attraction at short separations and fits a Morse-like potential at larger separation, and, third, the up-down solution becomes asymmetric at short distances, Fig. 4.

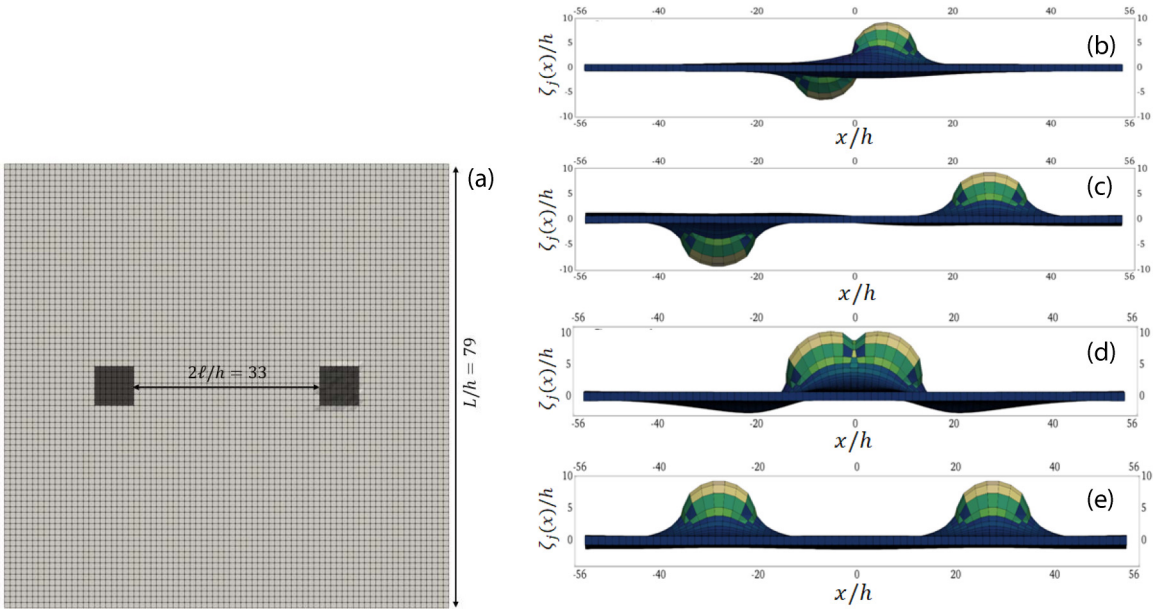

FIG. 5. Results of the gLSM simulations. (a) Top view of the initial setup. We consider a single layer of squared gel, $L\times L\times 1$, that is endowed with two squared inclusions (shaded areas). The distance between the closest edges of the inclusions is $2\ell/h$. We investigated two mutual separations, $2\ell/h = 33$ (shown in the figure) and $2\ell/h = 1$ (not shown). The results of these simulations are presented in panels (b)–(e). While panels (b) and (c) correspond to the up-down solution at large and small separations respectively, panels (d) and (e) correspond to the up-up scenario. Considering panels (c) and (e) we find that both solutions remain symmetric (either odd or even) around the center axis. Nonetheless, in the close separation the up-down solution (b) becomes asymmetric and the up-up solution (d) remains symmetric.

Although our system was not previously investigated within the FFT region of the parameter space, some experimental and numerical data on closely related systems are given in Refs. [11,48]. For example, the experimental study in Ref. [11] embedded two circular inclusions with dilative eigenstrains inside a narrow strip of gel, i.e., the external dimensions of the strip were of the order of the inclusion's radii. The authors reported that on actuation, the inclusions buckled spontaneously in the same direction, i.e., the energetically preferred pattern is the up-up solution. Contrary, the up-down scenario in this experiment was observed only with some initial interference. Indeed, this experimental result is in contradiction with our numerical solution that points to the up-down solution as the energetically preferable pattern. One possible resolution to this contradiction may be the fact that different regions in phase space have different global minimizers, i.e., the magnitude of the eigenstrains, the thickness of the material, and the overall dimensions of the plate affect the experimentally observed pattern. Indeed, the numerical study in Ref. [48] considered the interaction between two unit cells of a corrugated surface as a function of a normalized thickness [Fig. 5(k) in that paper]. Although the latter surface did not involve a discontinuous swelling profile, it nonetheless presented the same set of up-up and up-down solutions. The authors showed that the up-down solution becomes energetically preferable over the up-up case if the thickness is made small enough.

We emphasize that our work can provide guidelines in the design of patterned surfaces as, for example, is considered in Ref. [10]. In this paper, thin layers of hydrogels were patterned with periodic structures of circular inclusions. On actuation, each inclusion buckled upwards or downwards to relieve the stored elastic energy. The morphology of the buckled surface depended strongly on three major parameters: the relative distance between the inclusions, the relative spatial orientation of the inclusions, and the magnitude of the eigenstrains. We hypothesize that if this system is designed to operate within the FFT region of the parameter space, i.e., where localized buckling is favorable energetically, then knowing the characteristic length scale, ℓ_D, over which the interaction energy decays to zero will be useful for optimizing the behavior of the system. On one hand, if the relative separation between the edges of the inclusions is made large compared to ℓ_D, i.e., $(\ell - R)/\ell_D \gg 1$, then the inclusions will not interact at all, and buckling will occur randomly without any preferred direction. On the other hand, if $(\ell - R)/\ell_D \ll 1$, then we would expect the resulting morphology to exhibit a patterned surface with more ordered geometry. This ordered structure essentially will signify the mutual elastic cooperation between the inclusions. Nonetheless, we note that gels are more complicated systems than thin elastic plates, and therefore some corrections must be taken under consideration in the analytic calculations of ℓ_D (see discussion in Appendix A of Ref. [32]).

In summary, although the present study provided us some answers regarding the long-range interaction between buckled structures in thin elastic sheets, many questions yet remained open. Besides the analytical challenge to model the short-ranged interaction between two inclusions, it will be interesting to investigate the interaction energy between three or more of such isolated structures. Furthermore, it would be of great interest to study the post buckling behavior of circular inclusions with negative eigenstrains [10,38] or elongated inclusions that mimic fiber reinforces in organic materials [14].

ACKNOWLEDGMENTS

We acknowledge financial support from the DOE under Grant No. DE-FG02-90ER45438. This research was supported in part by the University of Pittsburgh Center for Research Computing through the resources provided.

APPENDIX A: ESSENTIAL FORMULAS IN CARTESIAN COORDINATES

In this Appendix we provide the essential formulas in the Cartesian representation. Following the formulation of the problem in Sec. II the reference metric is given by

$$\bar{g}_{\alpha\beta} = h(\mathbf{r})^2(dx^2+dy^2), \quad h(\mathbf{r}) = \begin{cases} \Phi & \mathbf{r}\in \text{inclusions} \\ 1 & \mathbf{r}\in \text{matrix} \end{cases}, \tag{A1}$$

where (x, y) are our set of Cartesian coordinates, see Fig. 1(a). The final 3D configuration is given by

$$\begin{aligned}\mathbf{f}(x,y) = &\left[\sqrt{g_{xx}}x + u_x^j(x,y)\right]\hat{\mathbf{x}} \\ &+ \left[\sqrt{g_{yy}}y + u_y^j(x,y)\right]\hat{\mathbf{y}} + \zeta_j(x,y)\hat{\mathbf{z}},\end{aligned} \tag{A2}$$

where $\sqrt{g_{xx}} = \sqrt{g_{yy}} = \Phi$ and $u_x^j(x,y)$, $u_y^j(x,y)$, and $\zeta_j(x,y)$ are the displacements in the x, y, and z directions, respectively. In addition, by the standard notation the unit vectors $\hat{\mathbf{x}}$, $\hat{\mathbf{y}}$, and $\hat{\mathbf{z}}$ form an orthonormal coordinate system. The polar and the Cartesian displacements are related by $u_r = u_x\cos\theta + u_y\sin\theta$ and $u_\theta = -u_x\sin\theta + u_y\cos\theta$.

While the total elastic energy, Eq. (3), remains unchanged compared to the polar representation, the stretching and bending energies, Eqs. (4), are transformed into

$$E_s^j = \frac{1}{2}\iint \sigma_{\alpha\beta}^j\epsilon_{\alpha\beta}^j dxdy, \tag{A3a}$$

$$E_b^j = \frac{1}{2}\iint M_{\alpha\beta}^j\phi_{\alpha\beta}^j dxdy, \tag{A3b}$$

where the indices α, β account for the two in-plane coordinates, x and y, and repeated indices imply summation. The stresses and the bending moments, $\sigma_{\alpha\beta}^j$ and $M_{\alpha\beta}^j$, are related to the "bending strains" by the same linear relations introduced in Sec. II. The transformation between the polar and Cartesian stresses are well known and given, for example, in Ref. [49, p. 24]. Nonetheless, the strain-displacement relations are modified into [24]

$$\epsilon_{\alpha\beta}^j = \tfrac{1}{2}\left(\partial_\alpha u_\beta^j + \partial_\beta u_\alpha^j + \partial_\alpha\zeta_j\partial_\beta\zeta_j\right), \tag{A4a}$$

$$\phi_{\alpha\beta}^j = \partial_{\alpha\beta}\zeta_j. \tag{A4b}$$

The equilibrium equations are obtained once we substitute these strain-displacement relations back in the energy, Eqs. (A3) and (3), and minimize it with respect to the displacements, u_x^j, u_y^j, and ζ_j. This gives

$$\partial_\alpha\sigma_{\alpha\beta}^j = 0, \tag{A5a}$$

$$B\Delta^2\zeta_j - \sigma_{\alpha\beta}^j\phi_{\alpha\beta}^j = 0, \tag{A5b}$$

where $\Delta = \partial_{xx} + \partial_{yy}$ is the Laplacian operator in Cartesian coordinates. Last, Eqs. (A5a) are automatically satisfied when

$$\sigma_{xx}^j = \partial_{yy}U^j, \quad \sigma_{yy}^j = \partial_{xx}U^j, \quad \sigma_{xy}^j = -\partial_{xy}U^j, \tag{A6}$$

where $U^j(x,y)$ are the Airy's stress functions. Similarly to Eq. (10) the compatibility equations for the stress functions $U^j(x,y)$ are

$$\Delta^2U^j = -\tilde{E}h\left[\phi_{xx}^j\phi_{yy}^j - \left(\phi_{xy}^j\right)^2\right]. \tag{A7}$$

APPENDIX B: DERIVATION OF EQS. (14)

In this section we derive Eq. (14). The derivation follows the analysis in Ref. [41, Ch. 5] and is extended to include corrections due to bending deformations. We emphasize that in this derivation the height functions, $\zeta_j(r,\theta)$, are assumed to be known.

The solutions to Eq. (10) are given by $U^j = U_h^j + U_p^j$, where U_h^j and U_p^j are the homogeneous and particular solutions, respectively. While the homogeneous solution satisfies the biharmonic equation, $\Delta^2U_h^j = 0$, the particular solution satisfies Eq. (10). Therefore, the function U^j satisfies both the equilibrium equations, Eq. (10), and the boundary conditions, Eqs. (7a) and (7c) in the radial and azimuthal directions, and Eqs. (11).

Let us start with the derivation of Eq. (14a), i.e., we aim to find $u_r^j(r,\theta)$ and $u_\theta^j(r,\theta)$ as a function of $U^j(r,\theta)$ and $\zeta_j(r,\theta)$. To do this, we first invert the stress-strain relations into $\epsilon_{rr} = (\sigma_{rr} - \nu\sigma_{\theta\theta})/\tilde{E}h$ and $\epsilon_{\theta\theta} = (\sigma_{\theta\theta} - \nu\sigma_{rr})/\tilde{E}h$ and substitute these inversions in Eqs. (5a) and (5c). Using the relations between the stresses and $U^j(r,\theta)$, Eqs. (9), we obtain,

$$\partial_r u_r^j = -\frac{1+\nu}{\tilde{E}h}\partial_{rr}U^j + \frac{1}{\tilde{E}h}\Delta U^j - \frac{1}{2}(\partial_r\zeta_j)^2, \tag{B1a}$$

$$\frac{1}{r}\partial_\theta u_\theta^j = -\frac{1+\nu}{\tilde{E}h}\left(\frac{1}{r}\partial_r U^j + \frac{1}{r^2}\partial_{\theta\theta}U^j\right) + \frac{1}{\tilde{E}h}\Delta U^j - \frac{u_r^j}{r} - \frac{1}{2r^2}(\partial_\theta\zeta_j)^2. \tag{B1b}$$

Second, we substitute $\Delta U^j = \Delta U_h^j + \Delta U_p^j$ into Eqs. (B1) and replace the homogeneous part of this term by

$$\Delta U_h^j = 4(\cos\theta\partial_r p_j + \sin\theta\partial_r q_j) = \frac{4}{r}(\cos\theta\partial_\theta q_j - \sin\theta\partial_\theta p_j), \tag{B2}$$

where $p_j(r,\theta)$ and $q_j(r,\theta)$ are conjugate harmonic functions, i.e., they satisfy the Cauchy-Riemann equations. Third, we substitute the first part of Eq. (B2) in Eq. (B1a) and integrate with respect to r,

$$u_r^j = -\frac{1+\nu}{\tilde{E}h}\partial_r U^j + \frac{4}{\tilde{E}h}(\cos\theta p_j + \sin\theta q_j) + \int\left[\frac{1}{\tilde{E}h}\Delta U_p^j - \frac{1}{2}(\partial_r\zeta_j)^2\right]dr. \tag{B3}$$

Similarly, we substitute Eq. (B3) along with the second part of Eq. (B2) in Eq. (B1b) and integrate with respect to θ,

$$u_\theta^j = -\frac{1+\nu}{\tilde{E}h}\frac{1}{r}\partial_\theta U^j + \frac{4}{\tilde{E}h}(\cos\theta q_j - \sin\theta p_j) + \frac{1}{\tilde{E}h}\int \left(r\Delta U_p^j\right)d\theta$$
$$- \iint\left[\frac{1}{\tilde{E}t}\Delta U_p^j - \frac{1}{2}(\partial_r\zeta_j)^2\right]drd\theta - \frac{1}{2r}\int(\partial_\theta\zeta_j)^2 d\theta. \tag{B4}$$

Multiplying Eq. (B4) by i and adding to Eq. (B3) gives

$$\frac{\tilde{E}h}{1+\nu}\left(u_r^j + iu_\theta^j\right) = -\left(\partial_r U_h^j + i\frac{1}{r}\partial_\theta U_h^j\right) + \frac{4}{1+\nu}(p_j + iq_j)e^{-i\theta} + u_\zeta^j(r,\theta)e^{-i\theta}, \tag{B5a}$$

$$u_\zeta^j(r,\theta) \equiv -e^{i\theta}\left(\partial_r U_p^j + i\frac{1}{r}\partial_\theta U_p^j\right) + \frac{e^{i\theta}}{1+\nu}\left(\int \Delta U_p^j(dr + ird\theta) - i\iint \Delta U_p^j drd\theta\right)$$
$$- \frac{\tilde{E}he^{i\theta}}{2(1+\nu)}\left[\int(\partial_r\zeta_j)^2 dr + \frac{i}{r}\int(\partial_\theta\zeta_j)^2 d\theta - i\iint(\partial_r\zeta_j)^2 drd\theta\right]. \tag{B5b}$$

Fourth, the most general homogeneous solution of Eq. (10) is given by $2U_h^j = (\bar{z}+\ell)\phi_j(z) + (z+\ell)\overline{\phi_j(z)} + \chi_j(z) + \overline{\chi_j(z)}$, where $\phi_j(z) = p_j + iq_j$ and $\chi_j(z)$ are arbitrary functions of the complex variable, z. Differentiation of the latter solution with respect to r and θ gives

$$\partial_r U_h^j + i\frac{1}{r}\partial_\theta U_h^j = [\phi_j(z) + (z+\ell)\overline{\phi_j'(z)} + \overline{\psi_j(z)}]e^{-i\theta}, \tag{B6}$$

where $\psi(z) \equiv \chi'(z)$. Substituting Eq. (B6) into Eq. (B5), and multiplying the resulting expression by $e^{i\theta}$, we obtain,

$$\frac{\tilde{E}h}{1+\nu}\left(u_r^j + iu_\theta^j\right)e^{i\theta} = \frac{3-\nu}{1+\nu}\phi_j(z) - (z+\ell)\overline{\phi_j'(z)} - \overline{\psi_j(z)} + u_\zeta^j. \tag{B7}$$

This equation recovers Eq. (14a) in the main text given that $u_\zeta^j = \frac{e^{i\theta}}{1+\nu}(r\partial_{rr}U_p^j - \nu\partial_r U_p^j)$. Indeed, it is straightforward to verify that Eq. (B5b) reduces to the latter expression in the case of an axisymmetric height function [50].

In a similar way we derive Eqs. (14b) and (14c). The starting point of this derivation requires us to calculate the total force in the radial and azimuthal directions, F_r and F_θ, over arbitrary curve on the plate,

$$ie^{i\theta}(F_r + iF_\theta) = e^{i\theta}\left(\partial_r U^j + i\frac{1}{r}\partial_\theta U^j\right) = \phi_j(z) + (z+\ell)\overline{\phi_j'(z)} + \overline{\psi_j(z)} + \sigma_\zeta^j, \tag{B8a}$$

$$\sigma_\zeta^j \equiv e^{i\theta}\left(\partial_r U_p^j + i\frac{1}{r}\partial_\theta U_p^j\right), \tag{B8b}$$

where in the second equality of Eq. (B8a) we used $U^j = U_h^j + U_p^j$ and Eq. (B6). The derivation of Eqs. (14b) and (14c) follows on differentiation of Eqs. (B8), see Ref. [41, p. 113].

APPENDIX C: SOLUTION TO THE COMPLEX POTENTIALS

In this section we derive the solution to the complex potentials, $\phi_j(z)$ and $\psi_j(z)$, introduced in Eqs. (14). The derivation follows Ref. [17] but includes additional corrections due to the assumed height function. Since these potentials are analytic functions, i.e., they are functions of the coordinate z but not of $\bar{z}$, they can be expanded in Taylor and Laurent series,

$$\phi_I(z) = \sum_{k=0}^{\infty} c_k z^k, \quad \psi_I(z) = \sum_{k=0}^{\infty} d_k z^k, \tag{C1a}$$

$$\phi_M(z) = \sum_{k=1}^{\infty}[a_k z^{-k} + A_k(z+2\ell)^{-k}], \quad \psi_M(z) = \sum_{k=1}^{\infty}[b_k z^{-k} + B_k(z+2\ell)^{-k}], \tag{C1b}$$

where $\{c_k, d_k, a_k, b_k, A_k, B_k\}$ are arbitrary complex constants to be determined by the boundary conditions. Nonetheless, under our set of simplifying assumptions these unknown are all real.

Following the analysis in Ref. [17] it can be shown that the boundary conditions on the axis of symmetry, Eqs. (11), are automatically satisfied given that

$$A_k = (-1)^{k+1}a_k, \tag{C2a}$$

$$B_k = (-1)^{k+1}b_k. \tag{C2b}$$

These constants remain unchanged compared to the analysis of the flat state in Ref. [17], because the height function that we assumed is symmetric around $x = -\ell$. In order to satisfy the boundary conditions on the interface of the right inclusion, Eqs. (7a) and (7c) in the radial and azimuthal directions, we set $z = R\sigma$, where $\sigma = e^{i\theta}$, and use Eqs. (14a) [or, equivalently, Eq. (B7)] and (B8a) to obtain the following conditions on the boundary:

$$\frac{2\sigma_o z}{1+\nu} + \frac{3-\nu}{1+\nu}\phi_I(z) - (z+\ell)\overline{\phi_I'(z)} - \overline{\psi_I(z)} + u_\zeta^I = \frac{3-\nu}{1+\nu}\phi_M(z) - (z+\ell)\overline{\phi_M'(z)} - \overline{\psi_M(z)} + u_\zeta^M, \tag{C3a}$$

$$\phi_I(z) + (z+\ell)\overline{\phi_I'(z)} + \psi_I(z) + \sigma_\zeta^I = \phi_M(z) + (z+\ell)\overline{\phi_M'(z)} + \psi_M(z) + \sigma_\zeta^M, \tag{C3b}$$

where $\sigma_o = \tilde{E}h(\Phi-1)/2$. While the first equation, Eq. (C3a), guarantee the continuity of the surface, Eq. (7a), the second equation, Eq. (C3b), guarantees the continuity of the radial and the shear stresses, Eq. (7c). Note that the continuity of Eq. (B8a) on the boundary of the inclusion is equivalent to the continuity of the radial and the shear stresses, see Ref. [17].

The remaining unknown constants, $\{c_k, d_k, a_k, b_k\}$, are determined from Eqs. (C3) once they are expanded in powers of σ. To do this, we first substitute $z = R\sigma$ in the complex potentials and expand the second terms in Φ_M and ψ_M in powers of σ. This gives

$$\phi_I(z) = \sum_{k=0}^{\infty} c_k (R\sigma)^k, \quad \psi_I(z) = \sum_{k=0}^{\infty} d_k (R\sigma)^k, \tag{C4a}$$

$$\phi_M(z) = \sum_{k=1}^{\infty} a_k (R\sigma)^{-k} + \sum_{k=1}^{\infty}\sum_{j=0}^{\infty} A_k R^{-k} h_{k,j}\sigma^j, \quad \psi_M(z) = \sum_{k=1}^{\infty} b_k (R\sigma)^{-k} + \sum_{k=1}^{\infty}\sum_{j=0}^{\infty} B_k R^{-k} h_{k,j}\sigma^j, \tag{C4b}$$

where $h_{k,j} = (-1)^j \frac{(k+j-1)!}{(k-1)!\,j!}(R/2\ell)^{k+j}$. Second, we expand the functions u_ζ^j and σ_ζ^j in powers of σ,

$$u_\zeta^j(r=R,\theta) = \sum_{k=-\infty}^{\infty} u_j^k \sigma^k, \quad \sigma_\zeta^j(r=R,\theta) = \sum_{k=-\infty}^{\infty} \sigma_j^k \sigma^k. \tag{C5}$$

Third, we substitute Eqs. (C4) and (C5) back in the boundary conditions, Eqs. (C3), and equate coefficients of the same order in $\sigma^k (k = 0, \pm1, \pm2, \dots)$. This gives linear algebraic equations that need to be solved for the unknown constants.

The solution for c_k and d_k as a function of a_k and b_k is given by

$$c_0 = -\frac{1+\nu}{4}\left(\sigma_I^0 - \sigma_M^0 + u_I^0 - u_M^0\right) - \sum_{j=1}^{\infty}(-1)^j R^{-j} h_{j,0} a_j, \tag{C6a}$$

$$c_1 = -\frac{\sigma_o}{2} + \frac{1+\nu}{4R}\left(u_M^1 - u_I^1 + \sigma_M^1 - \sigma_I^1\right) - \sum_{j=1}^{\infty}(-1)^j R^{-j-1} h_{j,1} a_j, \tag{C6b}$$

$$c_k = -(k-2)\frac{a_{k-2}}{R^{2k-2}} - \ell(k-1)\frac{a_{k-1}}{R^{2k}} + \frac{b_k}{R^{2k}} + \frac{\sigma_M^k - \sigma_I^k}{R^k} - \sum_{j=1}^{\infty}(-1)^j R^{-j-k} h_{j,k} a_j, \qquad (k = 2, 3, \dots), \tag{C6c}$$

$$d_0 = -c_0 - \ell c_1 - 2R^2 c_2 + \sigma_M^0 - \sigma_I^0 + \sum_{j=1}^{\infty}(-1)^j R^{-j}\left[j\left(\frac{\ell}{R}h_{j+1,0} + h_{j+1,1}\right)a_j - h_{j,0}a_j - h_{j,0}b_j\right], \tag{C6d}$$

$$d_1 = \frac{a_1}{R^2} - 2\ell c_2 - 3R^2 c_3 + \frac{\sigma_M^{-1} - \sigma_I^{-1}}{R} + \sum_{j=1}^{\infty}(-1)^j R^{-j-1}\left[j\left(\frac{\ell}{R}h_{j+1,1} + h_{j+1,2}\right)a_j - h_{j,1}b_j\right], \tag{C6e}$$

$$d_k = \frac{a_k}{R^{2k}} - \ell(k+1)c_{k+1} - (k+2)R^2 c_{k+2} + \frac{\sigma_M^{-k} - \sigma_I^{-k}}{R^k} + \sum_{j=1}^{\infty}(-1)^j R^{-j-k}\left[j\left(\frac{\ell}{R}h_{j+1,k} + h_{j+1,k+1}\right)a_j - h_{j,k}b_j\right], \quad (k = 2, 3, \dots). \tag{C6f}$$

In addition, the coefficients a_k and b_k satisfy the following equations:

$$a_1 = \frac{(1+\nu)R}{4}\left(\sigma_I^{-1} - \sigma_M^{-1} + u_I^{-1} - u_M^{-1}\right), \tag{C7a}$$

$$b_1 = -\sigma_o R^2 - \sum_{j=1}^{\infty}(-1)^j R^{1-j}(h_{j,1} + j h_{j+1,0})a_j + \frac{(1+\nu)R}{2}\left(u_M^1 - \sigma_I^1\right) - \frac{R}{2}(1-\nu)\left(\sigma_M^1 - \sigma_I^1\right), \tag{C7b}$$

$$b_k = (k-2)R^2 a_{k-2} + \ell(k-1)a_{k-1} + \frac{(1+\nu)R^k}{4}\left(\bar{u}_M^k - \bar{u}_I^k\right) - \frac{(3-\nu)R^k}{4}\left(\sigma_M^k - \sigma_I^k\right), \quad (k = 2, 3, ...), \tag{C7c}$$

$$a_k = \frac{1+\nu}{4}R^k\left(\sigma_I^{-k} - \sigma_M^{-k} + u_I^{-k} - u_M^{-k}\right), \quad (k = 2, 3, \dots). \tag{C7d}$$

Solution to leading order

In this section we derive the relevant coefficients for our leading-order solution. To do this, we first substitute Eq. (13) into Eq. (10) and obtain the particular solutions of the Airy's stress functions,

$$U_p^I(r) = -\frac{A^2\tilde{E}h}{16(\alpha-1)}\left(\frac{r}{R}\right)^{2\alpha}, \quad U_p^M(r) = \frac{A^2\tilde{E}h}{16(\alpha+1)}\left(\frac{r}{R}\right)^{-2\alpha}. \tag{C8}$$

Second, we substitute Eqs. (C8) in u_ζ^j and σ_ζ^j, Eqs. (B5b) and (B8b), and calculate the resulting expression on the edge of the inclusion, $r = R$. Using our expansion in powers of σ, Eq. (C5), it is clear that only the $k = 1$ coefficients do not vanish. These coefficients read,

$$u_I^1 = \frac{\tilde{E}hA^2\alpha(1+\nu-2\alpha)}{8R(1+\nu)(\alpha-1)}, \quad u_M^1 = \frac{\tilde{E}hA^2\alpha(1+\nu+2\alpha)}{8R(1+\nu)(\alpha+1)}, \tag{C9a}$$

$$\sigma_I^1 = \frac{\tilde{E}hA^2\alpha}{8R(1-\alpha)}, \quad \sigma_M^1 = -\frac{\tilde{E}hA^2\alpha}{8R(1+\alpha)}. \tag{C9b}$$

Using these expressions in Eqs. (C6) and (C7), we obtain the following coefficients:

$$c_1 = -\frac{\sigma_o}{2} + \frac{\tilde{E}h\,\alpha^3A^2}{8(\alpha^2-1)R^2}, \quad \text{and} \quad c_k = 0 \quad \text{for all } k \neq 1, \tag{C10a}$$

$$d_0 = -\ell c_1 + \frac{b_1}{2\ell}, \quad d_1 = -\frac{b_1}{(2\ell)^2}, \quad \text{and} \quad d_k = -b_1(-1)^{k+1}(2\ell)^{-k-1}, \quad \text{for all } k \geqslant 2, \tag{C10b}$$

$$a_k = 0, \tag{C10c}$$

$$b_1 = -\sigma_o R^2 + \frac{\tilde{E}h}{4}\alpha A^2, \quad \text{and} \quad b_k = 0, \quad \text{for all } k \neq 1. \tag{C10d}$$

Substituting these coefficients in the complex potentials, Eqs. (C1), and using the sum of a geometric series to obtain a closed-form solution for $\psi_I(z)$ gives Eqs. (15) in the main text.

APPENDIX D: DERIVATION OF EQ. (17)

In this Appendix we derive Eq. (17). Since the bending energy, the second line in Eq. (17), remains unchanged compared to Eqs. (3) and (4b), we focus only on the derivation of the stretching term, i.e., the first two terms in Eq. (17).

Using Eqs. (3) and (4a) the stretching energy is given by

$$E_s = 2\left(E_s^I + E_s^M\right), \tag{D1a}$$

$$E_s^j = \frac{1}{2}\iint \sigma_{\alpha\beta}^j \epsilon_{\alpha\beta}^j r d\theta dr, \tag{D1b}$$

where the integrations in Eq. (D1b) are taken either over the area of the right inclusion or the area of the matrix to the right of the axis of symmetry. Substituting the constitutive relations, Eqs. (5), in Eq. (D1b), and integrating by parts terms that include the in-plane displacements, u_r^j and u_θ^j, gives

$$\begin{aligned} E_s^j = {} & \frac{1}{2}\iint\left[\frac{1}{r}\partial_r\left(rf_r^j\right) + \frac{1}{r}\partial_\theta f_\theta^j\right]rd\theta dr + \frac{1}{4}\iint\left[\sigma_{rr}^j(\partial_r\zeta_j)^2 + \frac{1}{r^2}\sigma_{\theta\theta}^j(\partial_\theta\zeta_j)^2 + \frac{2}{r}\sigma_{r\theta}^j\partial_r\zeta_j\partial_\theta\zeta_j\right]rd\theta dr \\ & - \frac{1}{2}\iint\left[\partial_r\left(r\sigma_{rr}^j\right) - \sigma_{\theta\theta}^j + \partial_\theta\sigma_{r\theta}^j\right]u_r^j d\theta dr - \frac{1}{2}\iint\left[\partial_\theta\left(r\sigma_{r\theta}^j\right) + \sigma_{r\theta}^j + \partial_\theta\sigma_{\theta\theta}^j\right]u_\theta^j d\theta dr, \end{aligned} \tag{D2}$$

where $f_r^j = \sigma_{rr}^j u_r^j + \sigma_{r\theta}^j u_\theta^j$ and $f_\theta^j = \sigma_{\theta\theta}^j u_\theta^j + \sigma_{r\theta}^j u_r^j$. Evidently, the second line in Eq. (D2) vanishes identically if the equilibrium equations, Eqs. (6a) and (6b), are satisfied. Substituting Eq. (D2) back in the stretching energy, Eq. (D1a), gives

$$\begin{aligned} E_s = {} & \sum_{j=\mathrm{I,M}}\iint\left[\frac{1}{r}\partial_r\left(rf_r^j\right) + \frac{1}{r}\partial_\theta f_\theta^j\right]rd\theta dr \\ & + \frac{1}{2}\sum_{j=\mathrm{I,M}}\iint\left[\sigma_{rr}^j(\partial_r\zeta_j)^2 + \frac{1}{r^2}\sigma_{\theta\theta}^j(\partial_\theta\zeta_j)^2 + \frac{2}{r}\sigma_{r\theta}^j\partial_r\zeta_j\partial_\theta\zeta_j\right]rd\theta dr. \end{aligned} \tag{D3}$$

Comparing Eq. (D3) with the first two terms in Eq. (17) we find that they coincide if the height function is axisymmetric, i.e., derivatives of ζ_j with respect to θ vanish identically, and if the following relation holds:

$$\sum_{j=\mathrm{I,M}} \iint \left[\frac{1}{r}\partial_r\left(r f_r^j\right) + \frac{1}{r}\partial_\theta f_\theta^j\right] r d\theta dr = (1-\Phi)R^2 \int_0^{2\pi} \sigma_{rr}^I(R) d\theta. \tag{D4}$$

Given our set of simplifying assumptions we indeed have that $\zeta_j(r,\theta) \simeq \zeta_j(r)$. Therefore, it is left to verify Eq. (D4). To do this, we use the divergence theorem in both the inclusion and the matrix. Keeping in mind that the boundary of the inclusion is given by $r = R$, and the boundaries of the matrix are $r = R$ and $x = -\ell$, we obtain,

$$\iint \left[\frac{1}{r}\partial_r\left(r f_r^I\right) + \frac{1}{r}\partial_\theta f_\theta^I\right] r d\theta dr = \int_0^{2\pi} f_r^I(R) R d\theta, \tag{D5a}$$

$$\iint \left[\frac{1}{r}\partial_r\left(r f_r^M\right) + \frac{1}{r}\partial_\theta f_\theta^M\right] r d\theta dr = -\int_0^{2\pi} f_r^M(R) R d\theta + \int_{-\infty}^{\infty} f_x^M(-\ell, y) dy, \tag{D5b}$$

where $f_x^M = \sigma_{xx}^M u_x^M + \sigma_{xy}^M u_y^M$. Adding Eqs. (D5a) and (D5b) and using the boundary conditions on the edge of the inclusion, Eqs. (7a) and (7c) in the radial direction, and on the axis of symmetry, Eq. (11), yields Eq. (D4). This completes the derivation of Eq. (17).

APPENDIX E: METHODOLOGY OF THE NUMERICAL ANALYSIS

In this Appendix we present the numerical scheme used in Sec. IV. This scheme follows the analysis in Refs. [34,46,51] but includes some corrections that allow us to satisfy the appropriate boundary conditions at the plate's edges.

To derive the numerical scheme we adopt three modifications compared to the formulation in Secs. II and III. First, we use the Cartesian representation as presented in Appendix A. Second, the equilibrium equations are solved over the entire area of the plate, not just to the right of the axis of symmetry, and, third, we use the step function $\theta(x,y) = h(\mathbf{r}) - 1$ to prescribe the swelling profile. Consequently, in this section we do not differentiate between the elastic fields in the matrix and the inclusion.

The algorithm consists of the following steps:

(1) Guess an initial height function $\zeta_0(x,y)$.

(2) Multiply the height function with a filter function, $\zeta_n(x,y) \to \zeta_n(x,y)F(x,y)$ [52], where $n = 0 \cdots N$ is the iteration number.

(3) Calculate the corresponding in-plane stresses using Fourier transform [34],

$$\sigma_{\alpha\beta}(x,y) = \frac{\tilde{E}h}{4\pi^2}\iint [(\Phi-1)\tilde{\theta} - \tilde{k}_g/\xi^2] \times (n_\alpha n_\beta - \delta_{\alpha\beta}) e^{i\boldsymbol{\xi}\cdot\mathbf{x}} d\xi_x d\xi_y, \tag{E1}$$

where $\boldsymbol{\xi} = (\xi_x, \xi_y)$ is a two-dimensional wave vector, $\xi = (\xi_x^2 + \xi_y^2)^{1/2}$ is the vector's norm, $(n_x, n_y) = \boldsymbol{\xi}/\xi$ is a unit vector oriented in the direction of $\boldsymbol{\xi}$, and $\delta_{\alpha\beta}$ is the Kronecker delta. In addition, $\tilde{\theta}(\xi_x,\xi_y)$ and $\tilde{k}_g(\xi_x,\xi_y)$ are the Fourier transforms of the unit step functions $\theta(x,y)$ and the Gaussian curvature $k_g(x,y) = \phi_{xx}\phi_{yy} - \phi_{xy}^2$.

(4) Advance the height function in time using the Ginzburg-Landau equation $\partial_t \zeta = -\Gamma \frac{\delta E}{\delta \zeta}$, where Γ is a kinetic coefficient, and use the semi-implicit spectral method to calculate the height function in the next iteration [53],

$$\tilde{\zeta}_{n+1} = \frac{\tilde{\zeta}_n + \Gamma \Delta t (\sigma_{\alpha\beta}\phi_{\alpha\beta})_\xi}{1 + \Delta t \Gamma B \xi^4}. \tag{E2}$$

Here $\tilde{\zeta}_{n+1}(\xi_x,\xi_y)$, $\tilde{\zeta}_n(\xi_x,\xi_y)$, and $(\sigma_{\alpha\beta}\phi_{\alpha\beta})_\xi$ are the Fourier transforms of $\zeta_{n+1}(x,y)$, $\zeta_n(x,y)$, and $\sigma_{\alpha\beta}\phi_{\alpha\beta}$, respectively.

(5) Convert $\tilde{\zeta}_{n+1}(\xi_1,\xi_2)$ back to the real space $\zeta_{n+1}(x,y)$.

(6) Given the new height function, $\zeta_{n+1}(x,y)$, compute the total elastic energy, Eqs. (3) and (4), and go back to step 2. These iterations are repeated until the elastic energy converges to within the required accuracy.

This method has several advantages and disadvantages compared to the standard approach [54]. The main benefits are as follows: (i) Reduced computational time. The time step in the semi-implicit spectral method is significantly larger compared to Euler's scheme [53] (we choose $\Gamma\Delta t = 10^5$). (ii) Given the height function, we utilize the linearity of Eqs. (10) to obtain the exact solution for the in-plane stresses, Eq. (E1). Consequently, we solve the three-dimensional evolution of the plate by advancing in time only a single degree of freedom. These two benefits allow us to increase the number of grid points significantly while maintaining reasonable time frames for running the simulations. We prescribe 6.25×10^6 grid points and the number of iterations are $\sim 2\times10^6$. With a standard eight-core machine and appropriate parallelization of the code we obtain convergence to the eighth significant digit after approximately 48 h.

On the other hand, the main disadvantages of the method are as follows: (i) The numerical scheme is confined to the FvK model and does not account for elastic higher-order corrections that arise due to the discontinuity of the reference metric. (ii) Instead of free boundary conditions, Fourier transforms prescribe periodic boundary conditions on the plate's edges. Although the deformation decays to zero far from the plate's center, there are yet spurious nonzero stresses and bending moments on the plate's edges. For this reason, we prescribed the filter function, which is not required in the standard approach.

[1] J. D. Eshelby and R. E. Peierls, Proc. R. Soc. Lond. Ser. A **241**, 376 (1957).

[2] T. Mura, *Micromechanics of Defects in Solids*, 1st ed. (Matinus Nijhof, Amsterdam, 1982).

[3] A. Goriely, *The Mathematics and Mechanics of Biological Growth*, 1st ed. (Springer, Berlin, 2017).

[4] A. Goriely and M. Ben Amar, Phys. Rev. Lett. **94**, 198103 (2005).

[5] E. Hawkes, B. An, N. M. Benbernou, H. Tanaka, S. Kim, E. D. Demaine, D. Rus, and R. J. Wood, Proc. Natl. Acad. Sci. USA **107**, 12441 (2010).

[6] L. Ionov, Soft Matter **7**, 6786 (2011).

[7] J. Kim, J. A. Hanna, R. C. Hayward, and C. D. Santangelo, Soft Matter **8**, 2375 (2012).

[8] J. Kim, J. A. Hanna, M. Byun, C. D. Santangelo, and R. C. Hayward, Science **335**, 1201 (2012).

[9] Z. L. Wu, M. Moshe, J. Greener, H. Therien-Aubin, Z. Nie, E. Sharon, and E. Kumacheva, Nat. Commun. **4**, 1586 (2013).

[10] Z. J. Wang, C. N. Zhu, W. Hong, Z. L. Wu, and Q. Zheng, Sci. Adv. **3**, e1700348 (2017).

[11] Z. J. Wang, W. Hong, Z. L. Wu, and Q. Zheng, Angew. Chem. Int. Ed. **56**, 15974 (2017).

[12] N. Oppenheimer and T. A. Witten, Phys. Rev. E **92**, 052401 (2015).

[13] A. Plummer and D. R. Nelson, Phys. Rev. E **102**, 033002 (2020).

[14] R. M. Erb, J. S. Sander, R. Grisch, and A. R. Studart, Nat. Commun. **4**, 1712 (2013).

[15] S. Armon, E. Efrati, R. Kupferman, and E. Sharon, Science **333**, 1726 (2011).

[16] K. Zhou, H. J. Hoh, X. Wang, L. M. Keer, J. H. L. Pang, B. Song, and Q. J. Wang, Mech. Mater. **60**, 144 (2013).

[17] Z. Zou and S. Li, Acta Mech. **156**, 93 (2002).

[18] T. R. Weikl, M. M. Kozlov, and W. Helfrich, Phys. Rev. E **57**, 6988 (1998).

[19] H. Aranda-Espinoza, A. Berman, N. Dan, P. Pincus, and S. Safran, Biophys J. **71**, 648 (1996).

[20] A. Minami and K. Yamada, Eur. Phys. J. E **23**, 367 (2007).

[21] N. Dan, P. Pincus, and S. A. Safran, Langmuir **9**, 2768 (1993).

[22] C. Carraro and D. R. Nelson, Phys. Rev. E **48**, 3082 (1993).

[23] B. F. Grosso and E. J. Mele, Phys. Today **73**(9), 46 (2020).

[24] L. D. Landau and E. M. Lifshitz, *Theory of Elasticity*, 3rd ed. (Butterworth-Heinemann, Oxford, 1986).

[25] J. Dervaux and M. Ben Amar, Phys. Rev. Lett. **101**, 068101 (2008).

[26] E. Efrati, E. Sharon, and R. Kupferman, J. Mech. Phys. Solids **57**, 762 (2009).

[27] O. Oshri and H. Diamant, Phys. Rev. E **95**, 053003 (2017).

[28] B. Davidovitch, R. D. Schroll, D. Vella, M. Adda-Bedia, and E. A. Cerda, Proc. Natl. Acad. Sci. USA **108**, 18227 (2011).

[29] B. Davidovitch, R. D. Schroll, and E. Cerda, Phys. Rev. E **85**, 066115 (2012).

[30] D. Vella and B. Davidovitch, Phys. Rev. E **98**, 013003 (2018).

[31] H. King, R. D. Schroll, B. Davidovitch, and N. Menon, Proc. Natl. Acad. Sci. USA **109**, 9716 (2012).

[32] O. Oshri, S. Biswas, and A. C. Balazs, Phys. Rev. E **100**, 043001 (2019).

[33] Nonetheless, we showed that the discontinuity induced by the eigenstrains limits to the FvK model. Therefore, although the validity of the FFT solution is much wider than the NT solution, it is yet finite.

[34] L. Qiao, L. He, and Y. Ni, Inte. J. Solids Struct. **50**, 3742 (2013).

[35] O. Kuksenok, V. V. Yashin, and A. C. Balazs, Phys. Rev. E **78**, 041406 (2008).

[36] V. V. Yashin and A. C. Balazs, J. Chem. Phys. **126**, 124707 (2007).

[37] S. Biswas, V. V. Yashin, and A. C. Balazs, Soft Matter **14**, 3361 (2018).

[38] M. Pezzulla, S. A. Shillig, P. Nardinocchi, and D. P. Holmes, Soft Matter **11**, 5812 (2015).

[39] Y. Klein, E. Efrati, and E. Sharon, Science **315**, 1116 (2007).

[40] In Ref. [32] we defined this transition layer as the sum of the layers in the inclusion and the matrix. For this reason it included a factor of 2 compared to the current definition.

[41] N. I. Muskhelishvili, *Some Basic Problems of the Mathematical Theory of Elasticity*, 2nd ed. (Noordhoff International Publishing Leyden, Groningen, The Netherlands, 1975).

[42] S. Timoshenko and J. N. Goodier, *Theory of Elasticity*, 2nd ed. (Mcgraw–Hill, New York, 1951).

[43] E. H. Mansfield, *The Bending and Stretching of Plates*, 2nd ed. (Cambridge University Press, Cambridge, UK, 1989).

[44] Nonetheless, we note that other methods exist in the literature, such as the method of Green's functions [2], the Papkovich-Neuber displacement potentials [55], and the bipolar coordinates [56].

[45] A. Ardell and R. Nicholson, Acta Metall. **14**, 1295 (1966).

[46] Y. Ni, L. He, and Q. Liu, Phys. Rev. E **84**, 051604 (2011).

[47] O. Oshri, S. Biswas, and A. C. Balazs, Phys. Rev. E **99**, 033003 (2019).

[48] Y. Zhou, C. M. Duque, C. D. Santangelo, and R. C. Hayward, Adv. Funct. Mater. **29**, 1905273 (2019).

[49] M. A. Biot, *Mechanics of Incremental Deformations*, 1st ed. (John Wiley & Sons, New York, 1965).

[50] To show this reduction we first specialize Eqs. (10) to the case of axisymmetric height function, $\Delta^2 U_p^j = -\tilde{E}h\frac{1}{r}\partial_{rr}\zeta_j\partial_r\zeta_j$. Then we integrate this equation with respect to r obtaining, $(\partial_r\zeta_j)^2 = -\frac{2r}{\tilde{E}h}\partial_r\Delta U_p^j$. Substituting the latter relation in Eq. (B5b) and simplifying gives the required expression.

[51] K. Pan, Y. Ni, L. He, and R. Huang, Inte. J. Solids Struct. **51**, 3715 (2014).

[52] Since Fourier transform prescribes periodic boundary conditions on the system's edges, $\zeta_{n+1}(x, y)$ yet does not satisfy the boundary conditions of vanishing deformation on the plate's edges. For this reason, at each iteration we multiply the resulting height profile by a filter function, i.e., $\zeta_{n+1}(x, y) \to \zeta_{n+1}(x, y)F(x, y)$, that essentially equals 1 when $r < R_{\rm co}$ and decays to zero beyond it ($R_{\rm co} \gg R$). In our simulations we choose $F(x, y) = 1/[1 + (x^2 + y^2)^{2\alpha}/R_{\rm co}^{2\alpha}]$, where $R_{\rm co}/h = 850$. We verified numerically that the ultimate solution is neither sensitive to the particular selection of the filter function nor to the cut-off radius $R_{\rm co}$. This procedure essentially prescribes clamped boundary conditions on the edges. Nonetheless, since

the elastic profile is highly localized these boundary conditions neither effect the leading order of the observed pattern nor the energy of the interaction.

[53] L. Q. Chen and J. Shen, Comput. Phys. Commun. **108**, 147 (1998).

[54] H. S. Seung and D. R. Nelson, Phys. Rev. A **38**, 1005 (1988).

[55] M. Lee, I. Jasiuk, and E. Tsuchida, J. Appl. Mech. **59**, S57 (1992).

[56] G. B. Jeffery and L. N. G. Filon, Philos. Trans. R. Soc. Lond. Ser. A **221**, 265 (1921).